Homogeneous bubble nucleation in H2O- and H2O-CO2-bearing basaltic melts: results of high temperature decompression experiments

Nolwenn Le Gall, Michel Pichavant

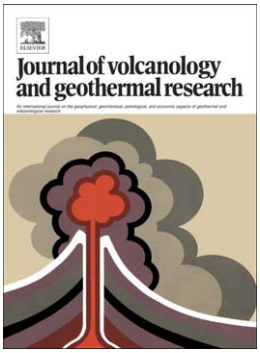

Homogeneous bubble nucleation in H_2O- and H_2O-CO_2-bearing basaltic melts: results of high temperature decompression experiments

Nolwenn Le Gall, Michel Pichavant

PII: S0377-0273(16)30381-X
DOI: doi:10.1016/j.jvolgeores.2016.10.004
Reference: VOLGEO 5940

To appear in: *Journal of Volcanology and Geothermal Research*

Received date: 1 December 2015
Revised date: 30 September 2016
Accepted date: 4 October 2016

Please cite this article as: Le Gall, Nolwenn, Pichavant, Michel, Homogeneous bubble nucleation in H_2O- and H_2O-CO_2-bearing basaltic melts: results of high temperature decompression experiments, *Journal of Volcanology and Geothermal Research* (2016), doi:10.1016/j.jvolgeores.2016.10.004

Homogeneous bubble nucleation in H_2O- and H_2O-CO_2-bearing basaltic melts: results of high temperature decompression experiments

Nolwenn Le Gall [a, *], **Michel Pichavant** [a]

[a] Université d'Orléans, ISTO, UMR 7327, 45071, Orléans, France, and CNRS/INSU, ISTO, UMR 7327, 45071, Orléans, France, and BRGM, ISTO, UMR 7327, BP 36009, 45060, Orléans, France

ABSTRACT

High pressure and temperature decompression experiments were conducted to provide experimental information on the conditions of homogeneous bubble nucleation in basaltic melts. Experiments were performed on H_2O- and H_2O-CO_2-bearing natural melts from Stromboli. Three starting volatile compositions were investigated: series #1 (4.91 wt.% H_2O, no CO_2), series #2 (2.37–2.45 wt.% H_2O, 901–1011 ppm CO_2) and series #3 (0.80–1.09 wt.% H_2O, 840–923 ppm CO_2). The volatile-bearing glasses were first synthesized at 1200°C and 200 MPa, and second continuously decompressed in the pressure range 150–25 MPa and rapidly quenched. A fast decompression rate of 78 kPa/s (or 3 m/s) was applied to limit the water loss from the glass cylinder and the formation of a H_2O-depleted rim. Post-decompression glasses were characterized texturally by X-ray microtomography. The results demonstrate that homogenous bubble nucleation requires supersaturation pressures (difference between saturation pressure and pressure at which homogeneous bubble nucleation is observed, ΔP_{HoN}) ≤ 50–100 MPa. ΔP_{HoN} varies with the dissolved CO_2 concentration, from << 50 MPa (no CO_2, series #1) to ≤ 50 MPa (872 ± 45 ppm CO_2, series #3) to < 100 MPa (973 ± 63 ppm CO_2, series #2). In series #1 melts, homogeneous bubble nucleation occurs as two distinct events, the first at high pressure ($200 < P < 150$ MPa) and the second at low pressure ($50 < P < 25$ MPa), just below the fragmentation level. In contrast, homogenous nucleation in series #2 and #3 melts is a continuous process. As well, chemical near-equilibrium degassing occurs in the series #1 melts, unlike in the series #2 and #3 melts which retain high CO_2 concentrations even for higher vesicularities (up to 23% at 25 MPa). Thus, our experimental observations underline a significant effect of CO_2 on the physical mechanisms of bubble vesiculation in basaltic melts. Our experimental decompression textures either reproduce or approach the characteristics of explosive basaltic eruptions, in terms of vesicularity, bubble shapes, sizes and number densities. Unimodal, exponential to power law bubble size distributions were encountered and correlated with the different melt series, textural characteristics and types of degassing.

Keywords:

Basalt

Degassing

Decompression

Volatiles

Bubble nucleation

Bubble size distribution

---

* Corresponding author at: ISTO, UMR 7327, 1A rue de la Férollerie, 45071, Orléans Cedex 02, France

E-mail address: nolwenn.le-gall@cnrs-orleans.fr (N. Le Gall)

1. Introduction

CO_2-supersaturated basaltic melts have been generated during experimental simulations of magma ascent and degassing (Pichavant et al., 2013), questioning the commonly accepted view that, due to their relatively high temperatures and low viscosities, basaltic magmas degas near equilibrium (Sparks et al., 1994). The classical degassing model implies that volatiles (mainly H_2O and CO_2) exsolve following solubility laws (e.g. Dixon and Stolper, 1995; Dixon et al., 1995), with CO_2 being extensively lost to the gas phase at high pressure (therefore earlier upon ascent) and H_2O negligibly lost until the latest stages of degassing (Blundy et al., 2010).

Further observations that imply deviation from equilibrium degassing either under simple open- (the gas phase escapes from the magma) or closed-system (the gas phase stays with the magma) include (1) the occurrence of CO_2-rich melt inclusions and (2) basaltic explosive volcanism.

(1) Melt inclusions having CO_2 contents higher than predicted from equilibrium H_2O-CO_2 degassing paths have been commonly found at basaltic volcanoes (e.g. Etna, Stromboli and Vesuvius volcanoes in Italy, Jorullo volcano in Mexico, Marianelli et al., 2005; Spillaert et al., 2006; Johnson et al., 2008; Métrich and Wallace, 2008; Métrich et al., 2010). These data have been interpreted mainly to result from the percolation of CO_2-rich magmatic fluids of deep provenance (Blundy et al., 2010). Alternatively, mixing of ascending and descending magmas (Witham, 2011; Beckett et al., 2014) could possibility generate melt inclusions with CO_2 contents displaced compared to calculated degassing trends. Lastly, Pichavant et al. (2013) proposed that the generation of CO_2-rich melts is possible during basaltic magma ascent and degassing, as a result of a disequilibrium degassing behavior of CO_2. So far, disequilibrium degassing is an idea accepted for silicic compositions, like phonolitic or rhyolitic melts (e.g. Gonnermann and Manga, 2005; Iacono-Marziano et al., 2007), but not really considered for basalts.

(2) Basaltic volcanoes are commonly characterized by effusive to low-intensity Hawaiian and Strombolian explosive eruptions (Sable et al., 2006; Costantini et al., 2010). However, some of these volcanoes (e.g. Etna, Stromboli, Tarawera in New Zealand and Masaya in Nicaragua) may erupt occasionally in high-intensity paroxysmal, subplinian to Plinian explosive eruptions (e.g. Sable et al., 2006, 2009; Costantini et al., 2010). Magma degassing is thought to play a fundamental role in determining effusive versus explosive eruptive behavior (Gonnermann and Manga, 2005); the transition is thought to depend on the regime of gas bubble transfer and to be caused by changes in magma supply and ascent rates (e.g. Pioli et al., 2008; Métrich and Wallace, 2008; Edmonds, 2008).

Magma degassing involves the nucleation, growth and coalescence of gas bubbles and has been studied via characterization of natural samples (e.g. Polacci et al., 2006, 2008, 2009; Shea et al., 2010), theoretical modeling (e.g. Toramaru 1989, 1995, 2006, 2014; Yamada et al., 2005) and laboratory experiments (e.g. Mourtada-Bonnefoi and Laporte, 1999; Mangan and Sisson, 2000; Mourtada-Bonnefoi and Laporte, 2002, 2004; Mangan and Sisson, 2005; Iacono-Marziano et al., 2007; Gardner and Ketcham, 2011). Experimental constraints are available for silicic melts, but are still lacking for basaltic melts. This type of work, which consists in determining when and how volatiles separate from magma, is nevertheless essential for the understanding of basaltic explosive volcanism (e.g. Bottinga and Javoy, 1990a; Herd and Pinkerton, 1997; Edmonds, 2008; Polacci et al., 2008; Gardner, 2012).

Although the experiments of Pichavant et al. (2013) were not specifically designed to study bubble nucleation, two characteristic distances controlling the degassing process of basaltic melts were identified: (1) the gas interface distance (distance between bubbles or to gas-melt interfaces at capsule walls) and (2) the volatile diffusion distance. In this way, on the basis of differing H_2O and CO_2 melt diffusivities, CO_2/H_2O concentration ratios may record nonequilibrium degassing (e.g. Gonnermann and Manga, 2005). Other studies have proposed that the rate of nucleation controls the final melt volatile concentrations through two fundamental parameters (Sparks 1978; Toramaru 1995; Cluzel et al., 2008): the pressure at which bubbles begin to nucleate and the number density of bubbles.

In line with these critical observations, continuous decompressions of H_2O- and H_2O-CO_2-bearing basaltic melts investigate the systematics of bubble nucleation, and improve our ability to model volatile evolution during magma ascent and degassing.

2. Theoretical background

During magma ascent and decompression, the melt can become supersaturated in volatiles. For a pressure (P) that becomes less than the volatile saturation pressure (P_{sat}), a critical level of volatile supersaturation is attained, and gas bubbles tend to nucleate to maintain chemical equilibrium. For homogeneous bubble nucleation to take place, a minimum pressure drop below P_{sat} is necessary (e.g. Mangan and Sisson, 2000; Mourtada-Bonnefoi and Laporte, 2002). In that case, bubbles are not associated with interfaces or discontinuities within the melt (for example at the surface of mineral phases or experimental capsule walls, e.g. Hurwitz and Navon, 1994; Gardner et al., 1999; Gardner and Denis, 2004; Mangan et al., 2004; Gardner, 2007; Cluzel et al., 2008), as for heterogeneous bubble nucleation, and high degrees of volatile supersaturation are theoretically required. According to the classical nucleation theory, the minimum supersaturation pressure (defined as the difference between the volatile saturation pressure and the pressure where bubbles start to nucleate homogeneously, ΔP_{HoN}) necessary for bubble nucleation is related to the surface tension of the bubble-melt interface (σ, in $N.m^{-1}$) and the nucleation rate (J, in $m^{-3}.s^{-1}$) according to the following expression (Hurwitz and Navon, 1994; Mourtada-Bonnefoi and Laporte, 2002):

$$\Delta P_{HoN} = (16\pi\sigma^3/3kT\ln(J/J_0))^{0.5} \quad (1)$$

where k is the Boltzmann constant ($1.38.10^{-23}$ $J.K^{-1}$), T is the temperature (in K) and J_0 is the preexponential nucleation rate (in $m^{-3}.s^{-1}$). J_0 is given by (e.g. Mourtada-Bonnefoi and Laporte, 2004):

$$J_0 = 2\Omega_L n_0^2 D_w/a_0(\sigma/kT)^{0.5} \quad (2),$$

where Ω_L is the volume of water molecules in the liquid ($\Omega_L = 3.10^{-29}$ m^3), n_0 is the number of water molecules per unit volume of liquid, a_0 is the mean distance between water molecules ($a_0 \approx n_0^{-1/3}$) and D_w is the water diffusivity in the liquid. n_0 is defined as $6.02.10^{23} X_m \rho_{liq}/m$, where $6.02.10^{23}$ is the Avogadro number, X_m is the mass fraction of molecular water in the liquid, ρ_{liq} is the liquid density (2650 kg/m^3), and m is the molar mass of water (0.018 kg/mol).

Eq. 1 indicates that homogeneous bubble nucleation in silicate melts can be viewed as a competition between volatile supersaturation (which tends to promote volatile exsolution) and the surface tension (which tends to resist the formation of a separate phase in the melt). The determination of the surface tension of silicate melts is difficult because it is highly sensitive to melt composition, temperature and dissolved volatile content (Bagdassarov et al., 2000; Mangan et al., 2004). The only data available for basaltic melts was determined by Khitarov et al. (1979) to range from 0.1 to 0.4 N.m^{-1} (the lowest end of the range for hydrous compositions at 1200°C). More recently, Pichavant et al. (2013) obtained σ ranging between 0.177 and 0.188 N.m^{-1} from the determination of ΔP_{HoN} and J, in decompression experiments on basaltic melts containing dissolved H_2O and CO_2. This is the approach followed in the present study to further constrain σ for basaltic melts, especially its dependence with the nature and concentration of dissolved volatiles.

Although the classical nucleation theory provides an adequate theoretical background for the experiments presented in this study, there are several specificities in our approach that are worth being outlined. First, natural basaltic magmas generally contain dissolved CO_2 and S species, in addition to H_2O. These volatile components have very contrasted individual solubilities in basaltic melts. It follows that conditions of melt saturation are not simply dependent on pressure (and of melt composition to some extent) but become a strong function of the respective dissolved volatile concentrations. The volatile saturation surface is no longer a line in pressure-H_2O concentration (e.g. Mourtada-Bonnefoi and Laporte, 1999, 2002) but an hypersurface in multicomponent space. In addition, degassing mechanisms take place at high temperature (> 1100°C) in basaltic melts, in a range where the diffusive mobility of volatiles (particularly H_2O, Zhang and Ni, 2010) is high and has a significant impact on the bubble nucleation process (e.g. Mangan and Sisson, 2000; Pichavant et al., 2013).

3. Experimental methods

3.1. Preparation of starting glasses

Decompression experiments were conducted on volatile-bearing glasses made from a Strombolian high-K basalt. The PST-9 "golden" pumice was used as starting material (Di Carlo et al., 2006; Pichavant et al., 2009, 2011). It was selected because it was previously used in phase equilibrium and crystallization experiments (Di Carlo et al., 2006; Pichavant et al., 2009, 2013), and because it is a sample well-characterized petrographically, mineralogically and geochemically (Pichavant et al., 2011). It is the most primitive golden pumice (Métrich et al., 2001; Bertagnini et al., 2003; Francalanci et al, 2004; Métrich et al., 2005; Di Carlo et al., 2006; Pichavant et al., 2009) and, as such, is representative of Stromboli pumices emitted during paroxysms and major explosions (Pichavant et al., 2011). Its bulk composition is given in Table 1. PST-9 is slightly porphyritic, containing about 10% of crystals of clinopyroxene, olivine and plagioclase, and lapilli are highly vesicular (~60 vol.% vesicles). To obtain a crystal- and bubble-free glass, the sample was hand-crushed to a fine powder, and then fused at 1 atm and 1400°C in a Pt crucible for 3 hours. This process gave a homogeneous glass whose composition is listed in Table 1. The glass was then either cored to cylinders (2.5 mm in diameter and about 10 mm long) or crushed to a fine powder (~10–50 µm).

For the synthesis experiments (Table 2), charges were made from glass cylinders (140.5–206.4 mg) or glass powder (about 30 mg). Using cylinders has the advantage of keeping a constant geometry in all samples, which facilitates the textural analysis. It also has the advantage of preventing the formation of bubbles in samples during the synthesis experiments. Nevertheless, glass powder was also used for practical reasons in a few experiments. Distilled water and carbon dioxide as silver oxalate ($Ag_2C_2O_4$) were added to generate volatile-bearing melts. $Au_{80}Pd_{20}$ capsules (2–3 cm height, 2.5 mm inner diameter, 0.2 mm wall thickness) were used as containers. Such a metal composition was adopted to minimize iron loss from the experimental charge to the capsule (Di Carlo et al., 2006; Pichavant et al., 2009). Three different proportions of H_2O and CO_2 were introduced in the capsules, corresponding to XH_2O_{in} (molar H_2O / (H_2O + CO_2)) = 1 (series #1: only H_2O

dissolved in glass, no CO_2 present), ~0.58 (series #2: H_2O and CO_2 both dissolved in glass, high dissolved H_2O/CO_2) and 0 (series #3: H_2O and CO_2 both dissolved in glass, low dissolved H_2O/CO_2, see below for the origin of H_2O).

For the decompression experiments (Table 3), the synthesized volatile-bearing glass cores (2.5 mm in diameter and about 4 mm long) were fitted in $Au_{80}Pd_{20}$ capsules. No additional volatile was introduced, and this resulted in low proportions of free fluid in the decompression charges. Capsules of identical diameter (2.5 mm) but variable lengths (up to 5 cm for the capsules decompressed to the lowest pressures) yielded variable and large void spaces to accommodate gas expansion during decompression.

All capsules were welded shut and weighed, and then reweighed after being placed several hours in an oven to ensure that no leaks occurred.

3.2. Equipment

Experiments were performed in an internally heated pressure vessel (IHPV) working vertically and fitted with a drop-quench device. To control the redox conditions, the vessel was pressurized with gas mixtures made of Ar and H_2. All synthesis and decompression experiments were performed with an initially applied pressure of 1 bar H_2. Then, Ar was pumped into the vessel up to the pressure needed to attain the final target conditions (Pichavant et al., 2013).

Determinations of experimental fH_2 have not been performed specifically for this study, for example with redox sensors (Taylor et al., 1992; Di Carlo et al., 2006). Below, we use fH_2 measurements made from Ni-NiPd sensors in similar experiments performed in the same IHPV and under the same *P*-*T*-fH_2 conditions (Le Gall and Pichavant, 2016). They indicate fO_2 conditions ranging from NNO–1.3 (series #3) to NNO+1.7 (series #1), NNO being the fO_2 of the Ni-NiO equilibrium at the *P*-*T* of interest.

The capsules were placed in a sample holder made of Al_2O_3. It was suspended by a thin Pt wire in a Mo furnace with a 2–3 cm long hotspot. Temperature was monitored with a Eurotherm controller and measured by two S-type thermocouples located along the capsules. Near-isothermal conditions (gradient < 2–3°C/cm) were maintained in the sample holder. Pressure and temperature were read continuously, with uncertainties of ± 20 bars and ± 5°C. At the end of the experiments, an electrical current was applied to the Pt suspension wire resulting in the sample holder falling to the cold part of the IHPV (< 100°C), leading to a quench rate of about 100°C/sec (Di Carlo et al., 2006).

3.3. Run procedure

The synthesis and decompression experiments (Tables 2 and 3) were generally performed independently from each other. Volatile-bearing melts were synthesized at a super-liquidus temperature of 1200°C (Di Carlo et al., 2006; Pichavant et al., 2009) and 200 MPa. Up to three capsules (one for each series#) were placed together in the vessel for durations of about 46–48 hours, in order to attain an equilibrium distribution of dissolved H_2O and CO_2 in the 2.5 mm diameter cores, according to the H_2O and CO_2 melt diffusion data (Zhang and Ni, 2010). The synthesized crystal- and bubble-free volatile-bearing glasses were then used as starting materials in the degassing experiments (Table 3).

The decompression runs also included up to three capsules. Experiments were conducted at a constant temperature of 1200°C, from an initial pressure (P_{in}) of 200 MPa to final pressures (P_f) varying between 150 and 25 MPa. All runs began with an approximately one-hour step at 200 MPa and 1200°C, to re-equilibrate the pre-synthesized glasses. Pressure was then decreased manually to P_f at a fast decompression rate of 78 kPa/s (equivalent to 3 m/s for an assumed rock density of 2650 kg/m^3), which leads to decompression durations of 10–40 min depending on P_f. Decompression charges were isobarically quenched immediately (within ~1–2 s) after attainment of P_f.

Less frequently, synthesis and decompression steps were conducted in the same run. This is the case of three synthesis + decompression experiments which were performed using glass powder as starting material (Table 4). Consequently, in those three cases, glasses were not analyzed after being synthesized. Each synthesis + decompression experiment included only one capsule from the series #1. The synthesis step lasted for about 40–60 min at 1200°C and 200 MPa, assuming that gas-melt equilibrium is attained in a matter of a few minutes under the experimental conditions investigated here (Zhang and Stolper, 1991; Lesne et al., 2011b) and using powders. Then, the continuous decompression-step consisted in a manual reduction of pressure until P_f was attained (150, 100 and 25 MPa) at a fast rate of 78 kPa/s.

After quenching, capsules were weighed again to check that no volatile loss occurred during the experiments, and then opened.

4. Analytical methods

4.1. Sample preparation

After each synthesis, a part of the glass core obtained was analyzed to check for its volatile concentration and distribution. Sections were cut perpendicular to the long axis of the glass cylinders and double-polished. Volatile concentrations were determined by the Fourier transform infrared spectroscopy (FTIR) technique.

After decompression, the glass cylinders were carefully removed from their containers and imaged in their entirety by X-ray microtomography. Then, glass cylinders were subdivided into several sections cut perpendicular to the cylinder long axis. One section (or several sections when additional analyses were needed) was doubly-polished for the determination of the glass volatile contents by FTIR. Another section (or small glass fragments) was mounted in epoxy resin and polished for scanning electron microscope (SEM) imaging.

4.2. Textural analyses

Textures of all decompressed charges were analyzed by X-ray computed tomography (X-ray CT), using a GE Sensing, phoenix|x-ray, Nanotom 180 from ISTO operated between 90 and 101 kV with variable filament currents (40–170 µA). Glass cylinders were mounted on carbon fiber rods with thermoplastic adhesive, and between 750 and 1100 two-dimensional projections were acquired as they rotated by 360° with a resolution of 2.42–3.91 µm. The reconstruction of the tomographic projections, using phoenix software, creates an image stack of the sample, which can be processed with ImageJ (Abràmoff et al., 2004) to obtain a complete three-dimensional reconstruction. The total reconstructed volume V consists in void space (v2), a glass volume (v3) and a bubble volume (v4) (Fig. 1a). The void space volume corresponds to the volume left when excluding the volume of the sample (v3 + v4) to the total volume investigated (e.g. v2 = V – (v3 + v4)). Both v2 and v4 can be measured using ImageJ. This allows the determination of v3 (by subtracting the sum of the volumes of void space (v2) and bubbles (v4) to the total volume investigated (V), v3 = V – (v2 +v4), Fig. 1a), and thus of the textural parameters (bubble size, bubble number density and vesicularity).

Image stacks (V, Fig. 1a) were segmented by manual thresholding; the objects of interest (bubbles and void space, in gray (for illustration) and black on Fig. 1a) were separated from the glass (in white on Fig. 1a). Following segmentation, the volume of these objects, all labeled and counted, was measured using the 3D Object Counter plugin (Bolte and Cordelières, 2006). The fact that thresholded objects are labeled allows rejecting particles which are artifacts, like cracks or noise. This was carefully done after each image analysis.

Bubble sizes (expressed as diameters) were determined from the measured bubble volumes, assuming a spherical shape. This assumption was found to be valid in most cases, except for the largest bubbles in glasses decompressed to 25 MPa (Fig. 4a–c), and for bubbles in series #1 glasses decompressed from powders (Table 4). *Bubble number density* (*BND*) was calculated as the number of bubbles per unit volume of bulk sample (glass + bubbles, *BND*, Tables 3 and 4) or per unit volume of melt (BND_{melt}, Tables 3 and 4). The BND_{melt} values were preferentially used because they remain invariant as bubbles grow (e.g. Proussevitch et

al., 2007). *Vesicularity* was calculated by dividing the measured bubble volumes by the combined volumes of melt and bubbles. As mentioned above, the volume of melt v3 depends on the void space volume v2, which includes open bubbles located at the rim of the glass cylinders. These bubbles were thus initially excluded from vesicularity measurements (V^c, Tables 3 and 4, Fig. 1a), resulting in significant underestimates for samples having large bubbly rims. To compensate for this issue, a sub-volume that included open edge bubbles (V_{sub}, Fig. 1b) together with Voxel Counter plugin was used instead of the total volume (V, Fig. 1a) and the 3D Object Counter plugin, yielding a more robust vesicularity value (V^d). V^d (given in tables 3 and 4 and used below in the text and figures) is the average of calculations performed on 4 representative regions in each sample.

For comparison with the vesicularities measured in our run products, equilibrium vesicularities were computed for the PST-9 melt composition. Two end-member cases were considered, corresponding to the degassing of pure H_2O and pure CO_2, respectively. The equilibrium vesicularity is given by (e.g. Cluzel, 2007):

$$V = (X_0 - X_s) / (X_0 - X_s + ((\rho_{fluid}/\rho_{liq})(1 - X_0))) \quad (3)$$

where X_0 is the weight fraction of initial water, X_s the solubility of the volatile species at a given pressure, ρ_{fluid} the density of the supercritical fluid and ρ_{melt} the density of the saturated silicate liquid.

The H_2O and CO_2 solubilities for PST-9 at 1200°C and the P of interest (25–200 MPa) were calculated based on the models of Lesne et al. (2011a, b). The density of the liquid is assumed to be constant and equal to 2.64 $g.cm^{-3}$ (with H_2O) and about 2.75 $g.cm^{-3}$ (with CO_2). The density of pure H_2O supercritical fluid was determined at the pressure of interest, using the Holloway-Flowers version of the Redlich-Kwong equation of state (from Holloway, 1981; Ferry and Baumgartner, 1987). For the pure CO_2 supercritical fluid, density was obtained from a regression of the fCO_2 data of Dixon et al. (1995) at 1200 °C.

4.3. Scanning electron microscopy

Scanning electron microscope (SEM) imaging was used for the observation of < 4 µm bubbles that cannot be resolved by X-ray microtomography. Samples were imaged using the MIRA3 TESCAN FEG instrument at Orléans, with an accelerating voltage between 15–25 kV. Results were used only to refine the appearance of bubbles (nucleation) and no attempt was made to extract quantitative textural data on the images.

4.4. Glass volatile contents

H_2O and CO_2 (as CO_3^{2-}) concentrations in the experimental glasses were determined by FTIR. A Nicolet 6700 spectrometer and a Continuµm IR microscope equipped with an IR source, a KBr beamsplitter and a liquid nitrogen cooled MCT/A detector were used together. Profiles with 50–350 µm steps were performed to check for the homogeneity of H_2O and CO_2 concentrations. The diameter of the analyzed spot was 50 µm, 100 µm in a few cases. FTIR spectra were accumulated for 128 scans at a resolution of 4 cm^{-1} on doubly polished samples, with thicknesses ranging between 29 and 171 µm (Table 5). H_2O and CO_2 concentrations were calculated from the Beer-Lambert law. For H_2O, the absorbance of the 3530 cm^{-1} total H_2O band (H_2O_{mol} + OH^-) was measured with a straight base line between ~3850 and ~2500 cm^{-1}. An extinction coefficient (ε^{3530}) of 64 $L.mol^{-1}.cm^{-1}$ was used (Dixon et al., 1995). For CO_2, the absorbance of the 1515 cm^{-1} carbonate ions band was determined on subtracted spectra. The spectrum used for the subtraction was obtained on a starting glass without dissolved volatiles. We calculated an extinction coefficient (ε^{1515}) of 363 $L.mol^{-1}.cm^{-1}$ from the equation of Dixon and Pan (1995). Sample thicknesses were measured with an optical microscope to within 1–2 µm. Densities of experimental glasses were estimated from the density of the volatile-free starting glass measured using a Mettler balance equipped with a density accessory kit (ρ = 2.747 ± 0.001) and considering a partial molar volume of H_2O of 12 $cm^3.mol^{-1}$ (Richet et al., 2000). In this way, we consider only the influence of dissolved H_2O on the glass density and assume that the effect of CO_2 is negligible (Lange, 1994; Bourgue and Richet, 2001; Lesne et al., 2011a).

5. Experimental results

5.1. Volatile contents of pre-decompression glasses

All glass cylinders obtained in the synthesis experiments (hereafter designated as pre-decompression glasses) were bubble-free. Considering the analytical uncertainty for CO_2 measurements (~100 ppm), glasses have homogeneous volatile contents. FTIR profiles reveal that H_2O and CO_2 are homogeneously distributed in the glass cylinders; near-rim volatile concentrations are identical within error to the other values (averaged H_2O and CO_2 contents in Tables 2 and 5). Pre-decompression glasses divide into three groups of compositions according to their synthesis conditions: series #1 (4.91 ± 0.01 wt.% H_2O, 0 ppm CO_2), series #2 (2.41 ± 0.04 wt.% H_2O, 973 ± 63 ppm CO_2) and series #3 (0.98 ± 0.16 wt.% H_2O, 872 ± 45 ppm CO_2). Their H_2O and CO_2 concentrations are within the range of experimental solubilities found both for PST-9 (Lesne et al., 2011a, b) and other basaltic melts (Shishkina et al., 2010) under similar *P*-*T* conditions. Although H_2O was not introduced in the series #3 capsules, it was found to be dissolved in all pre-decompression glasses of this series. This H_2O (concentration range: 0.80–1.09 wt.%, Tables 2 and 5) is generated during synthesis through the reduction of the ferric iron of the starting glass by H_2 from the pressurizing medium. The reduction reaction can be written (e.g. Lesne et al., 2011a):

$$Fe_2O_{3(melt)} + H_{2(vap/melt)} = 2FeO_{(melt)} + H_2O_{(melt)} \quad (4)$$

However, part of the water in the series #3 glasses most probably comes from the silver oxalate used as the CO_2 source because reaction (Eq. 4) is not sufficient to account for the measured glass H_2O contents.

Glasses from the few synthesis + decompression experiments (#1, Table 4) were not analyzed and are assumed to have the same water content as glass S9#1 (4.91 wt.%, Table 2) since the conditions of synthesis are identical (XH_2O_{in}, *P*, *T*). Water diffusivity data for basaltic melts (Zhang and Ni, 2010) suggest that, under the *P*-*T* conditions investigated here, a few minutes is sufficient to homogenize the H_2O concentration in our basaltic glasses, when starting from powder (Lesne et al., 2011b).

5.2. Qualitative textural characteristics of post-decompression glasses

The glass cylinders from the decompression experiments and from the few synthesis + decompression experiments (hereafter designated as post-decompression glasses) were generally recovered as single cylindrical blocks, except a series #1 charge (S+D38#1, Table 4) which yielded a partially powdered run product, suggesting partial fragmentation (as also described in Le Gall and Pichavant, 2016). Microscopic observation revealed the presence of numerous bubbles in the fragmented part of S+D38#1. All run products were crystal-free with the exception of the D25#3 charge (Table 3) which contains some plagioclase. These crystals (5–10 μm long) are found exclusively near bubbles (but not attached to) and are absent from bubble-free glass areas. In the other charges, the absence of crystals was checked by optical microscopy on the doubly polished sections prepared for FTIR and by SEM. Almost all the charges contain some rare oxide crystals (Ti-bearing magnetite, Di Carlo et al., 2006). However, evidence for bubble nucleation on those micron-sized Fe–Ti oxides was infrequently observed, as it can be seen on Fig. 2a. Except the D31#2 charge (Fig. 2b, Table 3) which is completely devoid of bubbles, the post-decompression glasses show a densely nucleated core and a bubbly rim ranging from ~10 to 110 μm (Fig. 2c, Tables 3 and 4). A distinction was made between bubbles that nucleated inside the glass and those located at the glass-capsule interface. The latter are thought to result from heterogeneous nucleation along the glass-capsule interface (Mangan and Sisson, 2000) and are not considered further in this study (with the sole exception of vesicularity measurements). Given the nearly uniform spatial distribution of interior bubbles and the absence of crystals (hence of possible nucleation sites), we interpret the textures of our vesiculated glasses to result from homogeneous bubble nucleation. Charge D31#3 is characterized by a somewhat heterogeneous distribution of relatively large bubbles (8–42 μm, Table 3). However, SEM imaging revealed a population of smaller bubbles (< 5 μm, Fig. 2a) almost homogeneously distributed.

Interiors of post-decompression glasses are devoid of bubbles until P_f = 150 MPa for series #1 and #3, and until P_f = 100 MPa for series #2. In this study, no experimental check was performed at P_f = 200 MPa but similar work at a lower decompression rate confirmed that bubbles are initially absent (Le Gall and Pichavant, 2016).

5.3. Quantitative study of internal textures

Vesicularities range from 1.01 to 25.6 vol.% (series #1), 0 to 22.7 vol.% (series #2) and from 0 to 4.97 vol.% (series #3) (Tables 3 and 4, Fig. 3a). They generally increase with decreasing P_f from 150 to 25 MPa, especially between 50 and 25 MPa. Vesicularities are also a function of the volatiles in the system (Fig. 3a). The highest vesicularities are for the H_2O-only glasses from series #1. For the same final pressure P_f = 25 MPa, vesicularities decrease with increasing CO_2 content from 25.6% (series #1) to 22.7% (series #2) to 4.97% (series #3). Vesicularities for series #2 and #3 glasses are in qualitative agreement with the calculated equilibrium vesicularity curves (since they plot in-between the two end-members theoretical curves, Fig. 3a). Measured vesicularities in the series #1 glasses are low by comparison to the theoretical values (Tables 3 and 4, Fig. 3a).

The average bubble diameter (*D*) ranges from 28 to 218 µm (series #1), 10 to 31 µm (series #2) and from 10 to 12 µm (series #3) (Tables 3 and 4, Fig. 3b). In the fragmented part of the series #1 S+D38#1 charge, bubbles have sizes ranging from about 10 to 110 µm, much lower than in the non-fragmented part (76–414 µm). As for vesicularity, *D* generally increases with decreasing P_f although to a lesser extent for series #3 glasses (Fig. 3b). *D* is also a function of the concentration of dissolved volatiles (Figs. 3b and 4a–c). For the same final pressure of 25 MPa, bubble sizes decrease with lowering H_2O content from 218 µm (series #1, Figs. 3b and 4a) to 31 µm (series #2, Figs. 3b and 4b) to 12 µm (series #3, Figs. 3b and 4c).

Bubble number densities (*BND*s) range from about 10^0 to 10^4 mm^{-3} for the three glass series (Tables 3 and 4, Fig. 3c). Generally, *BND*s of series #1 glasses decrease with decreasing P_f, from about 10^2 (150 MPa) to 10^1 mm^{-3} (25 MPa). Conversely, *BND*s of series #2 and #3 glasses generally increase when lowering P_f (from about 10^0 to 10^4 mm^{-3}), except between P_f = 100 and 50 MPa where *BND*s decrease.

For each series, the evolution of bubble size distribution (BSD) along the experimental decompression path is documented from two charges, one representative of the initiation and the other of the last stage of the bubble nucleation process (Fig. 4d–f). Each of the three series shows a distinct evolution of BSD with decreasing pressure and, so, increasing experimental duration. At P_f = 150 MPa, the CO_2-free glasses (series #1, Fig. 4d) show a unimodal BSD with a slight dissymmetry at left. Then, at P_f = 25 MPa (Fig. 4d), the BSD shifts to multimodal as the number of large bubbles increases. For example, at P_f = 150 MPa bubble sizes range from 8 to 86 µm while at P_f = 25 MPa bubble sizes range between 76 and 414 µm (Table 4, Fig. 4d). For series #2 samples, the BSD initially (at P_f = 100 MPa, i.e. at the pressure where bubbles start to nucleate) has a power law shape (Fig. 4e). Upon decreasing P_f to 25 MPa, the BSD evolves to an unimodal shape with a strong dissymmetry at left implying that the number of small bubbles (< 10 µm) decreases (Fig. 4e). Lastly, series #3 glasses have power law distributions both at P_f = 150 and 25 MPa (Fig. 4f), with small bubbles (< 10 µm) predominating until the lowest P_f.

5.4. Volatile contents of post-decompression glasses

H_2O and CO_2 concentrations in glasses from decompression experiments are reported in Table 5 and shown in Fig. 5. The H_2O concentrations of series #1 post-decompression glasses range from 4.16 (P_f = 150 MPa) to 1.71 wt.% (P_f = 25 MPa). Thus, a general decrease of the concentration of dissolved H_2O is observed when decreasing the final pressure (Fig. 5). Considering that standard deviations (corresponding to the error bars in Fig. 5) are < 0.1% (Table 5), the H_2O contents of series #1 post-decompression glasses are in close agreement with H_2O solubilities calculated from VolatileCalc (Newman and Lowenstern, 2002); the correspondence between the data points and the calculated 150–25 MPa isobars is very close (Fig. 5). However, the correspondence is slightly less good if comparison is made with measured solubilities (Lesne et al., 2011b) rather than with VolatileCalc, especially at low pressure: post-decompression glasses have H_2O concentrations slightly exceeding solubilities (Fig. 6a). Most series #1 charges have near-equilibrium H_2O concentrations. The exception is charge S+D38#1 (P_f = 25 MPa) which shows a supersaturation of 0.15–0.40 absolute wt.% H_2O. In addition, analytical dispersions of H_2O contents along FTIR profiles are higher than typical analytical errors, suggesting some degrees of heterogeneity in the H_2O distribution in

post-decompression glasses (Fig. 6a). The spatial distribution of H_2O in all series #1 charges seems influenced by the proximity of the glass-capsule interface, as illustrated for example by D10#1 and S+D38#1 samples (Fig. 6a). The glass H_2O concentration is also affected by the proximity to gas bubbles, which shows that the H_2O concentration is close to the solubility value near the bubbles or the glass-capsule interface and slightly higher away from them (Fig. 6a, b), consistent with a mechanism of diffusive motion of H_2O inside the melt toward the gas phase.

Series #2 post-decompression glasses have H_2O concentrations ranging from 1.96 to 0.95 wt.% and CO_2 concentrations ranging between 786 and 206 ppm (Table 5). Taken globally, concentrations of dissolved H_2O and CO_2 in post-decompression glasses progressively decrease with decreasing P_f (Fig. 5). However, the drop in H_2O concentration is not linear with P_f contrary to CO_2. For example, the glass decompressed to P_f = 150 MPa has a lower H_2O content (1.28 wt.%, D31#2) than two glasses decompressed to 100 (1.55 wt.%, D34#2) and 50 MPa P_f (1.96 wt.%, D9#2). The glass decompressed to 25 MPa (0.95 wt.%, D28#2) has the lowest H_2O concentration. Post-decompression glass CO_2 concentrations progressively decrease from 786 (D31#2, P_f = 150 MPa), 613–678 (D34#2 and D23#2, P_f = 100 MPa), 556 (D9#2, P_f = 50 MPa) to 206 ppm (D28#2, P_f = 25 MPa). The trend of decreasing H_2O and CO_2 concentrations upon decreasing pressure differs from the closed-system equilibrium decompression trend in that the observed H_2O loss is more important than theoretically expected. At P_f = 150 MPa, the measured CO_2 concentration is in agreement with the gas-melt saturation isobar calculated with VolatileCalc (Newman and Lowenstern, 2002) despite that the H_2O content is much lower than the concentration expected along the theoretical degassing trend. In comparison, the data points at P_f = 100 and 50 MPa plot well above their respective gas-melt saturation isobars. Measured CO_2 contents in these post-decompression glasses (556–678 ppm) largely exceed the calculated values (< 250 ppm at 100 MPa and < 50 ppm at 50 MPa) for closed-system equilibrium degassing, the departure from equilibrium being the most marked for the 50 MPa P_f point. The P_f = 25 MPa point also plots above its respective gas-melt saturation isobar.

Post-decompression glasses from series #3 have H_2O concentrations between 1.06 and 0.49 wt.% and CO_2 concentrations ranging from 777 to 423 ppm (Table 5). With decreasing pressure, melt CO_2 contents decrease progressively at approximately constant H_2O concentrations, except for charge D25#3 which lost most of its water (from 1.09 wt.% H_2O at 200 MPa to 0.49 wt.% H_2O at 25 MPa, Table 5 and Fig. 5). However, the decompressed glasses keep CO_2 concentrations that plot generally above their respective gas-melt saturation isobars. For example, the glass decompressed to P_f = 50 MPa has a higher CO_2 content (619 ppm, D9#3) than the calculated value (< 200 ppm) for closed-system equilibrium degassing. FTIR profiles show that H_2O and CO_2 are homogeneously distributed in the post-decompression glasses.

6. Interpretation and discussion of experimental observations

6.1. Supersaturation pressures required for homogeneous bubble nucleation

Two main arguments support the homogeneous nature of bubble nucleation in our samples. (1) The lack of crystals, with the exception of some rare Fe–Ti oxides, in our experimental charges implies that there are no or little discontinuities to serve as nucleation sites in the melts. Although we can miss the non-resolved oxides by X-ray CT, because of their small size, we estimated the proportion of heterogeneously nucleated bubbles to be negligible (i.e. for each charge less than a few % of total bubbles, see also Le Gall, 2015). (2) The quite homogeneous distribution of the bubbles within samples, when they appear (Fig. 2a, c), is consistent with a general rather than a local bubble nucleation mechanism (as would be observed if bubble nucleation occurs on capsule walls). In addition, there are variations neither in the average size nor in the number density of bubbles inside samples (away from capsule walls) once bubble nucleation takes place.

The supersaturation pressure required for homogenous bubble formation, i.e. the difference between the starting pressure ($P_{in} = P_{sat}$) and the final pressure at which bubbles begin to nucleate homogeneously, can be determined from our decompression experiments. We observed almost homogeneously distributed bubbles in the core of series #1 glasses

(initial melt H_2O concentration = 4.91 wt.%) from P_f = 150 MPa (S+D36#1, Table 4). However, the bubbles appear to have been formed at a much higher pressure. Indeed, most of the bubbles have a subspherical shape attesting of slight deformation after being formed. Furthermore, small bubbles (< 10 µm) are almost absent (2%, Fig. 4d) and bubble growth seems already efficient (main peak diameter of 25 µm, Table 4 and Fig. 4d). Accordingly, the supersaturation pressure required to nucleate bubbles homogeneously in our H_2O-bearing, CO_2-free, melts must be much less than 50 MPa (ΔP_{HoN} << 50 MPa). It should be noted that the 150 MPa P_f series #1 charge (S+D36#1) was obtained from powder starting materials which could have facilitated bubble nucleation, thus lowering ΔP_{HoN}. In the same way, the fact that bubbles are slightly deformed in charge S+D36#1 is interpreted to result from the use of starting powders instead of cylinders. The ΔP_{HoN} value determined for series #1 glasses (<< 50 MPa) is lower than supersaturation pressures found for more evolved compositions. For example, the degree of supersaturation required to trigger homogeneous bubble nucleation is ~60–90 MPa in dacite melts (H_2O ~5 wt.%, Mangan and Sisson, 2005; Gardner and Ketcham, 2011), ~100 MPa in phonolite (H_2O ~5 wt.%, Iacono-Marziano et al., 2007) and ~95–150 MPa in rhyolite melts (for ~5–7 wt.% H_2O, Mangan and Sisson, 2000; Mourtada-Bonnefoi and Laporte, 2004; Gardner and Ketcham, 2011). Therefore, ΔP_{HoN} values << 50 MPa as found in this study appear specific of basaltic compositions and suggest that bubble nucleation is an easy process taking place at low supersaturations in hydrous basaltic melts.

In series #2 (initial melt H_2O concentration = 2.37–2.45 wt.% and CO_2 = 901–1011 ppm), the charge decompressed to 150 MPa P_f (D31#2, Table 3) yielded a bubble-free glass by X-ray CT (Fig. 2b), which was confirmed by SEM examination. In contrast, the two charges decompressed to 100 MPa P_f (D23#2 and D34#2, Table 3 and Fig. 2c) contain small and nearly equal-sized bubbles (main peak diameters of 6–7 µm) uniformly distributed, suggesting that homogeneous bubble nucleation takes place between 150 and 100 MPa P_f. Therefore, a critical supersaturation pressure of 100 MPa maximum and 50 MPa minimum is inferred for our series #2 H_2O- and CO_2-bearing basaltic melts. For comparison, Pichavant et al. (2013) found a supersaturation pressure of 150 MPa maximum in their experiments performed on compositions similar to our series #2 melts. However, no data were given for P_f > 50 MPa, and so it cannot be excluded that, in their decompression experiments, homogeneous bubble nucleation would have started at pressures > 50 MPa, leading to ΔP_{HoN} << 150 MPa. A critical supersaturation pressure of 200 ± 100 MPa was found by Lensky et al.

(2006) for CO_2 bubbles in a synthetic mafic melt decompressed from 1.5 GPa, which is in the same range or larger than determined here for series #2 melts. However, it is worth specifying that Lensky et al. (2006) worked on nominally H_2O-free melts. For more evolved melts, ΔP_{HoN} values determined for H_2O- and CO_2-bearing rhyolitic melts (4.6 wt.% H_2O and 800–1100 ppm CO_2, Mourtada-Bonnefoi and Laporte, 2002) range from 160 to 350 MPa, significantly above our ΔP_{HoN} values for series #2 melts. Therefore, it appears that the influence of CO_2 in increasing supersaturation pressures and ΔP_{HoN} values is lower for basaltic than for rhyolitic melts.

In series #3 glasses (initial melt H_2O concentration = 0.8–1.09 wt.% and CO_2 = 840–923 ppm), bubbles begin to nucleate from P_f = 150 MPa (D31#3, Table 3, Fig. 2a). These bubbles are so small (< 5 µm) that they were mostly undetected by X-ray CT (smallest bubble size detected in D31#3: 8 µm). Thus, a critical ΔP_{HoN} of 50 MPa maximum is also inferred for the series #3 melts. These results confirm the relatively low supersaturation pressures and ΔP_{HoN} values for basaltic melts, even when H_2O-poor and CO_2-bearing.

Our experimental results for basaltic melts suggest that the H_2O concentration has a small and, in detail, a complex effect on the critical supersaturation pressure needed to overcome the nucleation barrier (expressed as the ΔP_{HoN} value). The H_2O-richer (4.91 wt.%, series #1) and the H_2O-poorer (0.98 ± 0.16 wt.%, series #3) melts require apparently the same range of ΔP_{HoN} values (either < or ~50 MPa). Nevertheless, ΔP_{HoN} differences between our three series can be masked by our relatively large P_f steps (50 MPa). In this sense, the available textural evidence for the series #1 melts suggests that ΔP_{HoN} is in fact much lower than 50 MPa. In contrast, for series #3 melts, textural evidence for bubble nucleation at P_f >> 150 MPa is lacking, suggesting that ΔP_{HoN} is in fact very close to 50 MPa. Comparison between results for series #1 and #3 implies a negative but small influence of the melt H_2O concentration on ΔP_{HoN}. However, the increase of ΔP_{HoN} observed between series #3 ($\Delta P_{HoN} \leq 50$ MPa, 0.98 ± 0.16 wt.% H_2O) and series #2 glasses (ΔP_{HoN} < 100 MPa, 2.41 ± 0.04 wt.% H_2O) is not in agreement with a linear decrease of ΔP_{HoN} with increasing the dissolved H_2O content. Our experiments do not reveal a systematic influence of the H_2O concentration on bubble nucleation in basaltic melts, as suggested for example in the case of rhyolitic melts (e.g. Gondé et al., 2011).

The presence of dissolved CO_2 has been considered to influence the degree of supersaturation required for homogeneous bubble nucleation. Although the individual influence of CO_2 is difficult to separate from H_2O (since the two volatile concentrations usually vary together in the experiments) there are indications for supersaturation pressures and ΔP_{HoN} are positively correlated with the melt CO_2 concentration (Mourtada-Bonnefoi and Laporte, 2002; Bai et al., 2008). In our experiments, ΔP_{HoN} appears to increase linearly (although moderately) with increasing the melt CO_2 content, from << 50 MPa (no CO_2, series #1) to ≤ 50 MPa (872 ± 45 ppm CO_2, series #3) to < 100 MPa (973 ± 63 ppm CO_2, series #2). Although other factors (redox state) would need to be considered, our experimental results for the three series are consistent with a moderately important inhibiting role of CO_2 on bubble nucleation in basaltic melts.

Melt-bubble surface tensions have been calculated from our experimentally-determined supersaturation pressures and nucleation rates computed from our measured bubble number densities and decompression timescales, using Eqs. 1 and 2. D_w was taken from the equation of Zhang and Ni (2010) which takes into consideration the effects of H_2O content and temperature. Ω_L and X_m parameters are poorly constrained in basalt melts and we have used the values given by Mourtada-Bonnefoi and Laporte (2004), determined for rhyolitic liquids. Checks were performed to evaluate their influence on the calculated results and found to be small (< 0.001 $N.m^{-1}$). In the same way, the choice of the D_w equation leads to very small (< 0.001 $N.m^{-1}$) differences in σ. Because our P_f steps are large (50 MPa) and so supersaturation pressures given are maxima, calculated surface tensions are upper limits. Results give σ values of 0.058–0.059 $N.m^{-1}$ for series #1 and #3 melts, respectively, and of 0.091 $N.m^{-1}$ for series #2 melts. For comparison, Khitarov et al. (1979) obtained surface tensions of 0.1 to 0.4 $N.m^{-1}$ for basaltic melts at 1200°C and 100–500 MPa, the lowest end of the range corresponding to hydrous compositions. Pichavant et al. (2013) fitted σ data from their decompression experiments performed on compositions similar to our series #2 melts. They found a maximum σ of 0.18 $N.m^{-1}$ higher than in this study but consistent with their higher ΔP_{HoN} values.

6.2. Physical mechanisms of degassing and textures

Below we discuss the physical mechanisms of degassing that occur in our experiments, from nucleation, growth and coalescence of gas bubbles to magma fragmentation. Emphasis is placed on textural differences between the three series of post-decompression glasses.

6.2.1. Vesicularities

The data for the three glass series show a general increase in vesicularity upon decompression due to magma ascent and decreasing P_f (Fig. 3a). More in detail, specificities appear between the different series (vesicularities of series #3 glasses are always very low below 5%). Vesicularities of CO_2-bearing melts are lower than those of H_2O-rich melts, but we note that our CO_2-bearing compositions have reduced melt H_2O concentrations compared to our H_2O-rich melts. It is also worth noting that for series #1 and #2 glasses, the increase in vesicularity is more important between P_f = 50 and 25 MPa. Our measured vesicularities never reach the range for Stromboli pumices which have values between 47 and 67% (Polacci et al., 2006). However, it is recalled that the series #1 25 MPa P_f sample is partially fragmented, suggesting that the measured vesicularity is a minimum. The progressive increase in vesicularity with decreasing P_f is consistent with a mechanism of progressive melt vesiculation which is associated with decompression. This melt vesiculation mechanism is the result of different sub-processes that include bubble nucleation, growth, coalescence and outgassing, up to fragmentation. These different sub-processes are examined below.

6.2.2. Nucleation events

Textural evidence (bubble size distributions and bubble number densities) can be used to distinguish between single vs. multiple bubble nucleation events (or pulses) in our experiments. In series #1 glasses, the presence of numerous (1908) bubbles in the charge decompressed to P_f = 150 MPa (S+D36#1, Table 4), as well as its unimodal BSD (Fig. 4d), imply that a single event of nucleation occurred at P_f > 150 MPa. Then, *BND* remains relatively constant from P_f = 150 to 100 MPa, and even decrease slightly (from 275 to 210 mm^{-3}, Table 4 and Fig. 3c). This plateau marks the end of this nucleation event (as supported by the lack of small (< 10 µm) newly formed bubbles at 100 MPa P_f), and the beginning of bubble growth, deformation and coalescence (e.g. Martel and Iacono-Marziano, 2015). Therefore, this event of nucleation appears to begin before P_f = 150 MPa and to end between P_f = 150 and 100 MPa, i.e. it is restricted to a narrow P_f range. In contrast, the presence of newly nucleated bubbles (< 5–110 µm) in the fragmented part of S+D38#1 sample (25 MPa P_f) is remarkable because it implies that a second bubble nucleation event occurs between P_f = 50 and 25 MPa. Thus, two distinct nucleation events take place in our H_2O-only melts (series #1), each restricted to narrow P_f intervals and both driven by melt H_2O supersaturation (Fig. 6a).

In series #2 samples, a strong increase of *BND* is observed from P_f = 150 (BND_{melt} = 0 mm^{-3}) to 100 MPa (BND_{melt} = 269–10331 mm^{-3}) (Table 3, Fig. 3c) which corresponds to the beginning of the homogeneous bubble nucleation process. Below 100 MPa, two cases are possible, either a continuous increase of the *BND* (D23#2) or a decrease of the *BND* (D34#2). The first case suggests the continuation of the same process of bubble nucleation below 100 MPa, an interpretation supported by the continuous increase in the number of bubbles, from 1692 (P_f = 100 MPa, D23#2), 11609 (P_f = 50 MPa, D9#2) to 16187 (P_f = 25 MPa, D28#2). In addition, bubble diameters give evidence for the appearance of small (< 10 µm) newly formed bubbles, and thus indicate the occurrence of secondary nucleation events. The second case is interpreted to reflect the combination of bubble coalescence and continuous bubble nucleation. The distance between bubbles in charge D34#2 is 28 µm, significantly lower (96 µm) than in the other charge (D23#2) for the same P_f, consistent with the possibility that

coalescence can take place, thus decreasing the *BND*. In both cases, the evolution below 50 MPa and down to 25 MPa P_f is marked by an increase of *BND*s which is interpreted as the continuation of the nucleation process.

In series #3 samples, as in series #2, the *BND* first increases from 150 to 100 MPa P_f (BND_{melt} = 4 to 836 mm^{-3}, Fig. 3c, Table 3). Then, it decreases at 50 MPa (BND_{melt} = 17 mm^{-3}) because of bubble coalescence (the number of bubbles is reduced from 5768 to 160, Table 3), before increasing again at 25 MPa (BND_{melt} = 8799 mm^{-3}). This increase is interpreted as the continuation of the same bubble nucleation process. This is supported by the observation that, as degassing continues, small (< 10 µm) bubbles begin to form along the decompression path from 150 to 25 MPa P_f. In addition, this indicates the occurrence of multiple nucleation events.

In series #2 and #3 post-decompression glasses, no *BND* stabilization (which would mark by a horizontal line in Fig. 3c) is observed. According to the classical nucleation theory, *BND* stabilization would reflect the end of a nucleation event (e.g. Toramaru, 2006). Consequently, the *BND* results for series #2 and #3 are consistent with a continuous, rather than limited to narrow P_f ranges, bubble nucleation, as observed in series #1 glasses and in other studies as well (e.g. Mourtada-Bonnefoi and Laporte, 2002; Cluzel et al., 2008). Continued multiple nucleation events have been proposed to yield power law distributions because small bubbles continue to form as volatile supersaturation is maintained (Blower et al., 2001, 2002; Yamada et al., 2005; Bai et al., 2008). This is precisely what is observed in series #2 and #3 which are both characterized by power law distributions (see below) and CO_2 melt concentrations in excess of the equilibrium solubilities.

We conclude to a major difference in the mechanism of bubble nucleation between series #1, on the one hand, and series #2 and #3, on the other hand. In series #1 glasses, a *discontinuous* mechanism of nucleation takes place, leading to two bubble nucleation events in narrow P_f intervals. Both nucleation events are driven by melt H_2O supersaturation. In contrast, in series #2 and #3 glasses, a single *continuous* mechanism of bubble nucleation occurs, leading to multiple discrete bubble nucleation pulses. In series #2 and #3, nucleation

takes place over a substantial P_f interval along the decompression path, and is driven by the generation of CO_2 supersaturated melts. Preservation of volatile supersaturated melts sustains continuous bubble nucleation during the entire duration of the decompression path.

In addition to differences concerning mechanisms of bubble nucleation between the three series, effects on bubble growth are also expected. It is likely that bubble growth occurs as a mechanism in our experiments in addition to bubble nucleation. The effect of bubble growth would be the most strongly marked in the longest decompression experiments, i.e. for the lowest P_f. We interpret the systematic differences in bubble size between the three series (Fig. 4a–c) to reflect the combined influence of bubble nucleation and growth. The largest bubbles are for the series #1 charge, followed by the series #2 and then the series #3 charges. Bubble growth is mainly controlled by volatile diffusion (Bai et al., 2008), as well as by gas volume expansion (larger at low pressures). H_2O having a higher melt diffusivity than CO_2 (Zhang and Ni, 2010), it is expected that bubbles would grow larger in series #1 than in series #2 and #3 if comparison is made at constant pressure so that the influence of gas volume expansion is neglected. The 25 MPa P_f charges (Fig. 4a–c) confirm this general trend since the highest bubble sizes occur in the series #1 charge.

6.2.3. Bubble coalescence

Bubble coalescence takes place in our H_2O-only glasses (series #1) although, in detail, differences appear along the decompression path. From P_f = 150 to 100 MPa, bubble coalescence is evidenced by a slight decrease of the bubble number density, from 275 (S+D36#1) to 210 mm^{-3} (S+D39#1, Table 4, Fig. 3c). Common coalescence structures of dimpling (Castro et al., 2012) are present in charge S+D36#1. In addition, the number of bubbles decreases from 150 (1908) to 100 MPa (776, Table 4) while, at the same time, the average and main bubble sizes increase (Table 4, Fig. 3b). Lastly, the evolution of the bubble size distribution from unimodal to exponential (see below) indicates the presence of larger bubbles interpreted to result from coalescence (Fig. 9a). Therefore, in series #1 glasses bubble coalescence begins very early along the decompression path.

Bubble coalescence is most extensively marked between 100 (S+D39#1) and 50 (D10#1) MPa P_f. This is evidenced by a sharp decrease of *BND* (from 210 to 8 mm^{-3}, Tables 3 and 4, Fig. 3c), a strong decrease in the number of bubbles (from 776 to 38, Tables 3 and 4) and a sharp increase in the average bubble size (from 47 to 161 µm, Tables 3 and 4, Fig. 3b). Processes of bubble deformation and coalescence are preserved in 50 MPa P_f, as well as in 25 MPa P_f charges, suggesting that the mechanism of bubble coalescence continues below 50 until 25 MPa P_f. In the latter charge, typical coalescence textures (Fig. 7) are characterized by deformed bubble walls, interpenetrating bubbles, dome-into-dimple shapes and vestiges of dimple structures, suggesting bending, stretching and dimpling mechanisms (Castro et al., 2012; Martel and Iacono-Marziano, 2015). It is worth mentioning that bubble coalescence is also observed in the fragmented parts of S+D38#1 sample. Bubble loss by buoyancy (outgassing) has to be considered, especially between 100 and 50 MPa P_f (contributing to lower *BND*s), although it must be limited by the short duration of the decompression (~11 min). Indeed, calculations of the gravity-driven upward movement of H_2O bubbles in charge S+D39#1 (which appears to be the most critically impacted by bubble loss), using the Hadamard-Rybcynski bubble velocity equation (Bottinga and Javoy, 1990b), give vertical travel distances of ~0.5–1 mm for bubbles of 50 µm diameter (and 7–18 mm for bubbles of 190 µm, bubble sizes from Table 4). Although the results depend sensitively on the bubble diameter, as well as on the gas density and the viscosity of the melt, they demonstrate that outgassing possibly occurs in our experiments, and can contribute to the loss of the larger bubbles and result in vesicularities below the equilibrium values.

In contrast with series #1, typical coalescence textures generally cannot be observed in series #2 and #3 glasses. In the absence of textural evidence, coalescence is demonstrated by a decrease of *BND*s and bubble numbers, associated with an increase in bubble sizes. In comparison, bubble growth would mark by a similar increase in bubble sizes, but at constant *BND*s and bubble numbers. Generally, coalescence is much less marked in CO_2-bearing than in CO_2-free melts. In series #2, coalescence is not systematic. *BND* values can either decrease or increase between 100 and 50 MPa P_f (Table 3, Fig. 3c). We interpret this difference to reflect variations in distances between bubbles in the two series #2 100 MPa P_f charges. The average distance between bubbles in charge D23#2 (96 µm) is larger than in charge D34#2 (28 µm), consistent with the absence of bubble coalescence when starting from a 100 MPa charge such as D23#2. Between 50 and 25 MPa P_f, the mechanism of bubble coalescence

continues despite an increase of the *BND* (Fig. 3c). However, coalescence textures were observed in a series #2 glass at P_f = 25 MPa (D28#2, Table 3). The mechanism of bubble coalescence is partially hidden by the continuing bubble nucleation.

We conclude that bubble coalescence occurs and that it is the more strongly marked in the same pressure range (100–50 MPa) for the three glass series.

6.2.4. Fragmentation

Fragmentation was observed (although partially) in one series #1 charge decompressed to P_f = 25 MPa, but never at P_f = 50 MPa. In an analogous way, Le Gall and Pichavant (2016) obtained several fragmented charges at the same P_f in slower (39 kPa/s) decompression experiments. Therefore, the available evidence suggests a fragmentation threshold near 25 MPa. A detailed discussion of the fragmentation mechanisms is outside the scope of this paper. However, our data, combined with those of Le Gall and Pichavant (2016), provide clear evidence that fragmentation is intimately related to the second bubble nucleation event that occurs between 50 and 25 MPa in series #1 melts. It is worth reminding that the small bubbles that result from the second nucleation event were observed only in the fragmented part of S+D38#1. The existence of a second nucleation event enhancing magma fragmentation has been previously proposed by e.g. Massol and Koyaguchi (2005).

6.3. Equilibrium vs. non-equilibrium degassing

Chemical equilibrium, as classically assumed for basaltic melts (Sparks et al., 1994), is reached or approached in our H_2O-only melts (series #1). Melts decompressed to 150, 100 and 50 MPa P_f exhibit near-equilibrium H_2O concentrations (Fig. 5). However, deviation from equilibrium is encountered in the charge decompressed to 25 MPa P_f (S+D38#1) which shows glass H_2O contents in slight excess (supersaturation of 0.15–0.40 wt.% absolute H_2O, Fig. 6) of the equilibrium solubility (Lesne et al., 2011b). Although this charge is particular (partially fragmented), we interpret our measured H_2O concentrations to indicate the

possibility of non-equilibrium degassing in series #1 melts at very low pressures, providing the driving force for the occurrence of the second bubble nucleation event. Despite chemical equilibrium being approached, textural equilibrium (defined by computed values of the volume fraction of bubbles expected from the equilibrium degassing of either a H_2O- or a CO_2-bearing basaltic melt, see Fig. 3a) is not reached in the series #1 melts which have vesicularities lower than expected from equilibrium degassing (Fig. 3a). This apparent contradiction between near-equilibrium melt H_2O concentrations and non-equilibrium vesicularities can be explained alternatively by a mechanism of diffusive motion of H_2O from inside the melt toward the gas phase (gas bubbles and capsule-melt interface) or by bubble outgassing. Concerning the former hypothesis, there is some evidence for H_2O diffusion in our series #1 samples (Fig. 6) but no indication for massive diffusive transfer of H_2O that would lead to H_2O loss out of melt cylinders. Texturally, no systematic bubble-depleted rims have been observed in our series #1 samples. About the latter hypothesis, bubble outgassing has been demonstrated above (see Bubble coalescence) to be operative in our experiments. We conclude that the lowering of our experimental vesicularities is mainly due to bubble outgassing.

Non-equilibrium degassing occurs systematically in the CO_2-bearing melts (series #2 and #3). CO_2 is retained within these melts at elevated concentration levels. In parallel, H_2O is lost in significant amounts. The combination of high melt CO_2 concentrations and H_2O losses generates a degassing trend that is in marked contrast with theoretical equilibrium closed-system degassing trends (Fig. 5). The unusual degassing trends observed in our experiments for the series #2 and #3 melts were previously found in the decompression experiments of Pichavant et al. (2013). The authors stressed the importance of two characteristic distances (the distance between bubbles and the volatile diffusion distance) in the control of the degassing process. This model attributes an important role to differences in diffusivities between the volatile components in the melt, as emphasized by Yoshimura (2015) who developed a diffusive fractionation model of H_2O and CO_2 degassing. As an illustration, at P_f = 50 MPa (D9#2), the calculated distance for CO_2 diffusion is only 150 µm in the time interval of the decompression experiment (Zhang and Ni, 2010) while the H_2O diffusion is 1060 µm, i.e. 7 times faster. In that charge the average distance between bubbles is 62 µm which would appear to be small enough for equilibrium degassing to be reached. However, this is not what is observed since CO_2 is kept at concentrations much higher than expected

along the 50 MPa isobar (Fig. 5). As an explanation, it is worth mentioning that the distance between bubbles is an average and also that there are large uncertainties on the timescales used for the diffusion distance calculations. Despite the general non-equilibrium behavior in all series #2 and #3 charges, the series #2 charge decompressed to P_f = 25 MPa (D28#2) approaches equilibrium CO_2 concentration. This charge is characterized by relatively large (31 µm) gas bubbles and a high vesicularity (23%). The glass CO_2 concentration vs. vesicularity plot (Fig. 8) shows a negative trend (Pichavant et al., 2013). In comparison, e.g. Cluzel et al. (2008) emphasized the importance of the *BND* parameter, the extent of degassing being positively correlated with the *BND*. However, our data show high and variable *BND*s correlated with large supersaturations in CO_2. Equilibrium degassing requires both numerous and large bubbles, i.e. the expression of a high vesicularity. This demonstrates that the mode of degassing and the textural parameters are related.

7. Volcanological applications

7.1. Comparison between experimental and natural textural parameters

Despite the fact that our experimental products do not simulate the last stages of degassing near the surface and post-fragmentation processes, the comparison of bubble textures between experimental and eruptive products can provide insights on degassing processes occurring in the volcanic conduit. The comparison focuses on products from three well-documented basaltic Plinian eruptions (Tarawera in 1886, Masaya and Etna in 122 BC, Sable et al., 2006, 2009; Costantini et al., 2010) and on products of Strombolian paroxysms (Polacci et al., 2006, 2009). At P_f = 25 MPa (i.e. at the pressure corresponding to the shallowest depth in our experiments, ~1 km), the H_2O-only charge (S+D38#1, Fig. 4a) exhibits a population of relatively large (76–414 µm) interconnected bubbles which are similar to the bubble-chains observed in products of the basaltic Plinian eruptions (Sable et al., 2006, 2009; Costantini et al., 2010). From our results, these bubble-chains would be generated by interaction between coalesced bubbles, in agreement with previous interpretations (Sable et al., 2006, 2009; Costantini et al., 2010). In addition, at P_f = 25 MPa, the CO_2-bearing charges (D28#2 and D25#3, Fig. 4b, c) exhibit a population of small (< 10 µm) to larger (up to 0.4 mm) bubbles. The products of basaltic Plinian eruptions and

Strombolian paroxysms also show a wide range of bubble sizes. The former have bubble sizes which range from 2–10 μm to 3–5 mm (Tarawera and Etna samples; Sable et al., 2006, 2009) up to 1.2 cm (Masaya samples; Costantini et al., 2010). The latter have a narrower range of bubble sizes ranging from 21–23 μm to 1 mm (Polacci et al., 2009). In both cases, the natural products exhibit larger bubbles than our experimental products. In the Plinian eruptions, the bubbles have either spherical to subspherical shapes or complex shapes (as discussed above). In contrast, the pumices from the paroxysmal Stromboli explosions display only the spherical to subspherical bubbles. From our results, the larger bubbles could have grown from high pressure, as a result of the combination of growth and coalescence processes. In contrast, the presence of small bubbles is always indicative of a mechanism of continuous nucleation occurring up to magma fragmentation, in agreement with the interpretation of Costantini et al. (2010). However, the absence of bubbles < 20 μm in the Strombolian pumices suggests that the mechanism of nucleation was ended before magma fragmentation. The lack of large (> 1 mm) bubbles with complex shapes implies that coalescence was not the dominant process, as observed in our CO_2-bearing charges.

Our experimental products have low vesicularities which extend up to 25.6% (series #1), 22.7% (series #2) and 4.97% (series #3). These values are much lower than the vesicularities measured in basaltic explosive products. For comparison, vesicularities of Strombolian pumices range from 47 to 67% (Polacci et al., 2006; Fig. 3a) and those of the Plinian products from the Masaya eruption are even higher, ranging between 70 and 78% (Costantini et al., 2010). It is reasonable to expect that the field of Stromboli pumices can be attained by extrapolating the data for the series #2 compositions to $P_f << 25$ MPa. For the H_2O-rich compositions, the 25 MPa P_f charge is partially fragmented and the measured vesicularity is a minimum.

The *BND*s found in Strombolian pumices ($6–9.10^2$ mm^{-3}, Polacci et al., 2009; Fig. 3c) are in the same range as the *BND*s measured in our CO_2-bearing run products (up to 10^4 mm^{-3} in series #2 and #3). In detail, at $P_f = 25$ MPa, the natural pumices have *BND*s lower by one order of magnitude than the series #2 and #3 charges. The H_2O-rich charges (series #1, Fig. 3c) are much less bubble-rich. The basaltic Plinian products from the Masaya eruption have *BND*s ($3–8.10^4$ mm^{-3}, Costantini et al., 2010) higher than all our experimental products.

We conclude that our decompression experiments either reproduce or approach the natural textures of explosive basaltic eruptions, in terms of vesicularity, bubble textures, sizes and number densities.

7.2. Use of BSD systematics

Below, we extend the comparison between our experimental products and the basaltic explosive products selected above to include BSDs. Vesicle size distribution is one of the most common textural parameters measured to understand processes of bubble nucleation and growth in natural products (e.g. Blower et al., 2001; Shea et al., 2010). Volcanic rocks are typically characterized by power law and exponential distributions of vesicle sizes (e.g. Gaonac'h et al., 1996; Bai et al., 2008; Polacci et al., 2009), but these were generally not reproduced in experiments, wherein a single event of nucleation is recorded and interactions between bubbles are limited (e.g. Lyakhovsky et al., 1996; Mourtada-Bonnefoi and Laporte, 1999; Gardner et al., 1999; Mourtada-Bonnefoi and Laporte, 2002; Cluzel et al., 2008), producing a unimodal BSD (Blower et al., 2002). However, in some experiments, products with BSDs more complex than unimodal have been encountered, such as in the study of Simakin et al. (1999), the analogue experiments of Blower et al. (2001, 2002) and in the degassing experiments of Bai et al. (2008, 2010, 2011), Polacci et al. (2008) and Masotta et al. (2014). Below, methods developed for the interpretation of natural BSDs are applied to our experimental results.

To do so, we have represented our experimental BSDs in cumulative number density plots, as commonly used (Fig. 9). These were obtained by regressing the number of bubbles per mm^3 against the bubble volume. In doing so, two main BSD types were encountered in our experimental samples: exponential and power law. Regressions were performed with Excel software. Very good fits were generally obtained yielding $R^2 > 0.99$ for more than 50% charges. One charge (S+D36#1) yielded a relatively poor exponential fit ($R^2 = 0.86$), consistent with its unimodal BSD (Figs. 4d, 9a).

The three post-decompression glass series show a different evolution of the BSD (Figs. 4d–f and 9). Upon decreasing P_f, the BSD of series #1 glasses evolves from a unimodal (S+D36#1, P_f = 150 MPa, Figs. 4d and 9a), mixed power law–exponential (S+D39#1, P_f = 100 MPa, Fig. 9a) to an exponential distribution (D10#1 and S+D38#1, P_f = 50–25 MPa, Fig. 9a). The mixed distribution recognized in charge S+D39#1 corresponds to two classes of bubble sizes. The small to medium bubbles (volumes ~10^2–10^5µm^3) can be fitted by an exponential function whereas the larger bubbles (volumes ~10^5–10^6µm^3) are best described by a power law with an exponent of 1.45. Texturally, it is clear that these large bubbles result from coalescence.

In series #2 samples, both power law and exponential bubble size distributions were observed when decreasing P_f from 100 to 25 MPa (Fig. 9b). At P_f = 100 MPa (i.e. at the pressure where bubbles start to nucleate), the BSDs of the two D23#2 and D34#2 duplicate charges are best described by power laws (Fig. 9b). In contrast, at P_f = 50 and 25 MPa, the BSDs in charges D9#2 and D28#2 can be described by mixed power law–exponential distributions: the small-to-medium sized bubbles can be fitted with an exponential relation (Fig. 9b) whereas the medium-to-large bubbles follow a power law relation. Series #2 power law exponents range from 0.78 to 2.24. The low and high values of the range are for the two duplicate charges decompressed to 100 MPa P_f. If the power law exponents of these two charges are averaged (α = 1.51), all series #2 power law exponents appear to be tightly grouped (1.38–1.62).

In series #3 post-decompression glasses (Fig. 9c), only power law distributions were observed when decreasing P_f from 150 to 25 MPa, with the exception of the medium-sized bubbles (volumes ~10^3–10^5µm^3) in the D9#3 charge (P_f = 50 MPa) which are best fitted with an exponential distribution (bubble coalescence effect). The series #3 glasses display power law exponents of 0.62 to 1.23, slightly lower than in series #2 glasses.

We conclude to a systematic change in the BSD evolution with decreasing P_f between the three glass series. The H_2O-rich, CO_2-free, post-decompression glasses (series #1) are the only ones with a unimodal distribution and also the only ones with exponential distributions for all classes of bubble sizes. In contrast, the CO_2-bearing post-decompression glasses (series #2 and #3) are characterized by power law distributions. Among the CO_2-bearing glasses, only the series #2 show a transition from a power law to a mixed power law–exponential distribution. Series #3 glasses are characterized by predominantly power law BSDs.

Two distinct mechanisms have been invoked to explain the occurrence of power law bubble size distributions in volcanic rocks. A mechanism of diffusive bubble growth, allowing "cascading" coalescence, was involved by Gaonac'h et al. (1996) whereas, according to Blower et al. (2001, 2002), such distributions would be more indicative of far-from-equilibrium degassing, leading to a mechanism of continuous bubble nucleation and multiple nucleation events (in the absence of bubble coalescence). Exponential distributions would result from steady-state bubble nucleation and growth and thus would imply near-equilibrium degassing (Baker et al., 2006; Bai et al., 2008).

In our experiments, a unimodal distribution was found in the H_2O-only melts at a high P_f (in S+D36#1, P_f = 150 MPa), the closest to the beginning of the nucleation mechanism. The latter takes place in a narrow P_f interval, leading to a single bubble nucleation event. The melt H_2O concentration in that charge is equal to the solubility. Therefore, the S+D36#1 charge provides evidence that a unimodal bubble size distribution implies gas-melt equilibrium, despite the fact that its vesicularity is significantly less than the theoretical value. Exponential distributions are also specific to the H_2O-only series whose post-decompression glasses have generally (except the partially fragmented charge S+D38#1) equilibrium melt H_2O concentrations. Again, our experimental data support the interpretation that exponential BSDs are generated by a system evolving under near-equilibrium conditions (Blower et al., 2001; Baker et al., 2006; Bai et al., 2008) despite vesicularities being lower than theoretical values. The evolution from a unimodal to an exponential distribution would thus result from post-nucleation mechanisms (growth and coalescence), leading to larger bubble sizes and lower bubble number densities. Power law distributions are specific to the CO_2-bearing charges which are characterized by a single mechanism of continuous nucleation, leading to

multiple bubble nucleation events. Small bubbles continue to form because the level of volatile supersaturation in the melts is maintained. This is consistent with the preservation of high out-of-equilibrium CO_2 concentrations in the glasses. Therefore, our data confirm the model of Blower et al. (2001, 2002) in that power law distributions are associated with far-from-equilibrium degassing. Mixed power law–exponential distributions would thus correspond to an intermediate case where bubble nucleation is dominated by a coalescence process.

On this basis, we examine below natural textures of the selected basaltic explosive eruptions above. The microtextural data available for those different explosive products exhibit a range of BSDs. The bubble size distributions of Plinian eruptions products (Sable et al., 2006, 2009; Costantini et al., 2010) follow power law trends with exponents of the order of 1.5 (when exponents are expressed as volume, Baker et al., 2012), i.e. in the range of our experimental power law exponents for the H_2O- and CO_2-bearing melts (series #2). In comparison, pumice samples from Strombolian paroxysmal explosions are best fit by mixed power law–exponential distributions with a power law exponent of 1.4 (Polacci et al., 2009), again as the experimental power law exponent of our 25 MPa P_f series #2 charge (D28#2). From our results, the power law distributions found for the Plinian products imply disequilibrium degassing, leading to continuous bubble nucleation and growth, in agreement with previous interpretation (Costantini et al., 2010). The mixed power law–exponential found in Strombolian pumices would be indicative of a system where coalescence is superimposed on a continuous bubble nucleation process. This would correspond to a disequilibrium degassing situation and to an evolution toward equilibrium (e.g. Polacci et al., 2009).

8. Conclusions

We have performed high pressure and temperature decompression experiments to study the systematics of homogeneous bubble nucleation in basaltic magmas. Compared to previous works (Lensky et al., 2006; Pichavant et al., 2013) this study is the first to provide systematic textural information along the decompression path for three series of volatile concentrations. The main conclusions are the following:

(1) Degrees of supersaturation required for homogeneous bubble nucleation (ΔP_{HoN}) are ≤ 50–100 MPa, weakly dependent on the melt H_2O concentration but possibly dependent on the melt CO_2 concentration. These ΔP_{HoN} are significantly lower than found for silicic melt compositions which stresses that bubble nucleation in basaltic magmas is comparatively easy.

(2) In the H_2O-rich melts, homogeneous nucleation occurs as two distinct events taking place in narrow P_f intervals. The first and most important nucleation of bubbles occurs at high P_f ($200 < P_f < 150$ MPa) and the second nucleation of bubbles is restricted to low P_f ($50 < P_f < 25$ MPa), in close association with fragmentation. In contrast, in the CO_2-bearing melts, a single continuous mechanism of nucleation occurs over a substantial P_f interval along the decompression path, leading to multiple bubble nucleation events.

(3) Post-nucleation mechanisms include bubble growth, coalescence and outgassing, and lead to larger bubble sizes and lower *BND*s. Specific bubble coalescence textures and progressive *BND* decreases were observed with decreasing P_f. In both H_2O-rich and CO_2-bearing melts, coalescence is the more strongly marked in the same pressure range of 100–50 MPa.

(4) Both near-equilibrium and disequilibrium degassing occur in our experiments. The former is associated with the H_2O-rich, CO_2-free, melts while the latter occurs systematically in the CO_2-bearing melts. Post-decompression glasses retain CO_2 concentrations much higher than equilibrium values. There is a systematic link between textures and mode of degassing (equilibrium vs. disequilibrium). Near-equilibrium degassing requires both numerous and large bubbles and so high vesicularities.

(5) Partial fragmentation occurred in one H_2O-rich charge decompressed to 25 MPa, intimately related to the second event of bubble nucleation.

(6) Our experiments underline a significant effect of CO_2 on mechanisms (ΔP_{HoN} values, vesicularities, bubble sizes and densities) of basaltic melt degassing. The main difference between CO_2-bearing and CO_2-free melts concerns the mechanism of nucleation, continuous vs. discontinuous in the case of CO_2-bearing vs. CO_2-free melts.

(7) Our experimental decompression textures approach the characteristics of basaltic products from explosive eruptions. Vesicularities, *BND*s, bubble textures and sizes bring constraints on degassing processes occurring in the conduit.

(8) Our experimental products exhibit different BSDs, unimodal, exponential and power law with the volatile series. A relation is established between mechanisms of melt degassing, textures, volatile concentrations and type of BSDs. This provides a test on existing BSD based models to interpret natural degassing mechanisms.

Acknowledgments

This project has been financially supported by the VUELCO (EC FP7) and DEGAZMAG (ANR 2011 Blanc SIMI 5-6 003-02) projects. We are very grateful to A. Burgisser for help with the X-ray microtomography analysis technique and to I. Di Carlo for assistance with SEM analyses. We thank M.J. Rutherford for his editorial work, as well as T. Shea and D.R. Baker for their detailed and constructive reviews which helped to improve the manuscript. Previous comments from D. Laporte were also highly appreciated.

References

Abràmoff, M.D., Magalhães, P.J., Ram, S.J., 2004. Image processing with ImageJ. Biophotonics international 11, 36–43.

Bagdassarov, N., Dorfman, A., Dingwell, D.B., 2000. Effect of alkalis, phosphorus, and water on the surface tension of haplogranite melt. American Mineralogist 85, 33–40.

Bai, L., Baker, D.R., Rivers, M., 2008. Experimental study of bubble growth in Stromboli basalt melts at 1 atm. Earth and Planetary Science Letters 267, 533–547. doi:10.1016/j.epsl.2007.11.063

Bai, L., Baker, D. R., Hill, R. J., 2010. Permeability of vesicular Stromboli basaltic glass: Lattice Boltzmann simulations and laboratory measurements, Journal of Geophysical Research 115, B07201. doi:10.1029/2009JB007047

Bai, L., Baker, D.R., Polacci, M., Hill, R. J., 2011. In-situ degassing study on crystal-bearing Stromboli basaltic magmas: Implications for Stromboli explosions: Geophysical Research Letters 38, L17309. doi: 10.1029/2011GL048540

Baker, D.R., Lang, P., Robert, G., Bergevin, J.-F., Allard, E., Bai, L., 2006. Bubble growth in slightly supersaturated albite melt at constant pressure. Geochimica et cosmochimica acta 70, 1821–1838.

Baker, D.R., Brun, F., O'Shaughnessy, C., Mancini, L., Fife, J.L., Rivers, M., 2012. A four-dimensional X-ray tomographic microscopy study of bubble growth in basaltic foam. Nature Communications 3:1135.

Beckett, F.M., Burton, M., Mader, H.M., Phillips, J.C., Polacci, M., Rust, A.C., Witham, F., 2014. Conduit convection driving persistent degassing at basaltic volcanoes. Journal of Volcanology and Geothermal Research 283, 19–35.

Bertagnini, A., Métrich, N., Landi, P., Rosi, M., 2003. Stromboli volcano (Aeolian Archipelago, Italy): An open window on the deep-feeding system of a steady state basaltic volcano. Journal of Geophysical Research 108, 2336. doi:10.1029/2002JB002146

Blower, J.D., Keating, J.P., Mader, H.M., Phillips, J.C., 2001. Inferring volcanic degassing processes from vesicle size distributions. Geophysical Research Letters 28, 347–350.

Blower, J.D., Keating, J.P., Mader, H.M., Phillips, J.C., 2002. The evolution of bubble size distributions in volcanic eruptions. Journal of Volcanology and Geothermal Research 120, 1–23.

Blundy, J., Cashman, K.V., Rust, A., Witham, F., 2010. A case for CO_2-rich arc magmas. Earth and Planetary Science Letters 290, 289–301.

Bolte, S., Cordelières, F.P., 2006. A guided tour into subcellular colocalization analysis in light microscopy. Journal of microscopy 224, 213–232.

Bottinga, Y., Javoy, M., 1990a. Mid-ocean ridge basalt degassing: Bubble nucleation. Journal of Geophysical Research 95, 5125-5131.

Bottinga, Y., Javoy, M., 1990b. MORB degassing: Bubble growth and ascent. Chemical Geology 81, 255–270.

Bourgue, E., Richet, P., 2001. The effects of dissolved CO_2 on the density and viscosity of silicate melts: a preliminary study. Earth and Planetary Science Letters 193, 57–68.

Castro, J.M., Burgisser, A., Schipper, C.I., Mancini, S., 2012. Mechanisms of bubble coalescence in silicic magmas. Bulletin of Volcanology 74, 2339–2352.

Cluzel, N., 2007. Simulation expérimentale de l'ascension et de la vésiculation des magmas rhyolitiques : application à la cinétique de nucléation des bulles et implications volcanologiques. Ph.D. Thesis, Univ. Clermont-Ferrand 2, France.

Cluzel, N., Laporte, D., Provost, A., Kannewischer, I., 2008. Kinetics of heterogeneous bubble nucleation in rhyolitic melts: implications for the number density of bubbles in volcanic conduits and for pumice textures. Contributions to Mineralogy and Petrology 156, 745–763. doi:10.1007/s00410-008-0313-1

Costantini, L., Houghton, B.F., Bonadonna, C., 2010. Constraints on eruption dynamics of basaltic explosive activity derived from chemical and microtextural study: the example of the Fontana Lapilli Plinian eruption, Nicaragua. Journal of Volcanology and Geothermal Research 189, 207–224.

Di Carlo, I., Pichavant, M., Rotolo, S.G., Scaillet, B., 2006. Experimental Crystallization of a High-K Arc Basalt: the Golden Pumice, Stromboli Volcano (Italy). Journal of Petrology 47, 1317–1343. doi:10.1093/petrology/egl011

Dixon, J.E., Pan, V., 1995. Determination of the molar absorptivity of dissolved carbonate in basanitic glass. American Mineralogist 80, 1339–1342.

Dixon, J.E., Stolper, E.M., 1995. An experimental study of water and carbon dioxide solubilities in mid-ocean ridge basaltic liquids. Part II: applications to degassing. Journal of Petrology 36, 1633–1646.

Dixon, J.E., Stolper, E.M., Holloway, J.R., 1995. An experimental study of water and carbon dioxide solubilities in mid-ocean ridge basaltic liquids. Part I: calibration and solubility models. Journal of Petrology 36, 1607–1631.

Edmonds, M., 2008. New geochemical insights into volcanic degassing. Philosophical Transactions of the Royal Society A: Mathematical, Physical and Engineering Sciences 366, 4559–4579. doi:10.1098/rsta.2008.0185

Ferry, J.M., Baumgartner, L., 1987. Thermodynamic models of molecular fluids at the elevated pressures and temperatures of crustal metamorphism. Reviews in Mineralogy and Geochemistry 17, 323–365.

Francalanci, L., Tommasini, S., Conticelli, S., 2004. The volcanic activity of Stromboli in the 1906–1998 AD period: mineralogical, geochemical and isotope data relevant to the understanding of the plumbing system. Journal of Volcanology and Geothermal Research 131, 179–211. doi:10.1016/S0377-0273(03)00362-7

Gaonac'h, H., Stix, J., Lovejoy, S., 1996. Scaling effects on vesicle shape, size and heterogeneity of lavas from Mount Etna. Journal of Volcanology and Geothermal Research 74, 131–153.

Gardner, J.E., 2007. Heterogeneous bubble nucleation in highly viscous silicate melts during instantaneous decompression from high pressure. Chemical Geology 236, 1–12. doi:10.1016/j.chemgeo.2006.08.006

Gardner, J.E., 2012. Surface tension and bubble nucleation in phonolite magmas. Geochimica et Cosmochimica Acta 76, 93–102. doi:10.1016/j.gca.2011.10.017

Gardner, J.E., Denis, M.-H., 2004. Heterogeneous bubble nucleation on Fe-Ti oxide crystals in high-silica rhyolitic melts. Geochimica et Cosmochimica Acta 68, 3587–3597. doi:10.1016/j.gca.2004.02.021

Gardner, J.E., Ketcham, R.A., 2011. Bubble nucleation in rhyolite and dacite melts: temperature dependence of surface tension. Contributions to Mineralogy and Petrology 162, 929–943. doi:10.1007/s00410-011-0632-5

Gardner, J.E., Hilton, M., Carroll, M.R., 1999. Experimental constraints on degassing of magma: isothermal bubble growth during continuous decompression from high pressure. Earth and Planetary Science Letters 168, 201–218.

Gondé, C., Martel, C., Pichavant, M., Bureau, H., 2011. In situ bubble vesiculation in silicic magmas. American Mineralogist 96, 111–124. doi:10.2138/am.2011.3546

Gonnermann, H., Manga, M., 2005. Nonequilibrium magma degassing: Results from modeling of the ca. 1340 A.D. eruption of Mono Craters, California. Earth and Planetary Science Letters 238, 1–16. doi:10.1016/j.epsl.2005.07.021

Herd, R.A., Pinkerton, H., 1997. Bubble coalescence in basaltic lava: its impact on the evolution of bubble populations. Journal of Volcanology and Geothermal Research 75, 137–157.

Holloway, J.R., 1981. Volatile Interactions in Magmas, in: Newton, R.C., Navrotsky, A., Wood, B.J. (Eds.), Thermodynamics of Minerals and Melts, Advances in Physical Geochemistry. Springer New York, pp. 273–293.

Hurwitz, S., Navon, O., 1994. Bubble nucleation in rhyolitic melts: Experiments at high pressure, temperature, and water content. Earth and Planetary Science Letters 122, 267–280.

Iacono-Marziano, G., Schmidt, B.C., Dolfi, D., 2007. Equilibrium and disequilibrium degassing of a phonolitic melt (Vesuvius AD 79 "white pumice") simulated by decompression experiments. Journal of Volcanology and Geothermal Research 161, 151–164. doi:10.1016/j.jvolgeores.2006.12.001

Johnson, E.R., Wallace, P.J., Cashman, K.V., Granados, H.D., Kent, A.J., 2008. Magmatic volatile contents and degassing-induced crystallization at Volcán Jorullo, Mexico: implications for melt evolution and the plumbing systems of monogenetic volcanoes. Earth and Planetary Science Letters 269, 478–487.

Khitarov, N.I., Lebedev, E.B., Dorfman, A.M., Bagdasarov, N.S., 1979. Effect of temperature, pressure and volatiles on the surface tension of molten basalt. Geochemistry International 16, 78–86.

Le Gall, N., 2015. Basaltic magma ascent and degassing – Experimental approach, 318 p. Ph.D. thesis, University of Orléans.

Le Gall, N., Pichavant, M., 2016. Experimental simulation of bubble nucleation and magma ascent in basaltic systems: implications for Stromboli volcano. American Mineralogist 101, 1967–1985. doi:10.2138/am-2016-5639

Lange, R.A., 1994. The effect of H_2O, CO_2, and F on the density and viscosity of silicate melts. In: Carroll, M.R., Holloway, J.R. Eds., Volatiles in Magmas. Mineral. Soc. Am. Rev. in Mineral. 30, pp. 331–369.

Lensky, N.G., Niebo, R.W., Holloway, J.R., Lyakhovsky, V., Navon, O., 2006. Bubble nucleation as a trigger for xenolith entrapment in mantle melts. Earth and Planetary Science Letters 245, 278–288.

Lesne, P., Scaillet, B., Pichavant, M., Beny, J.-M., 2011a. The carbon dioxide solubility in alkali basalts: an experimental study. Contributions to Mineralogy and Petrology 162, 153–168.

Lesne, P., Scaillet, B., Pichavant, M., Iacono-Marziano, G., Beny, J.-M., 2011b. The H_2O solubility of alkali basaltic melts: an experimental study. Contributions to Mineralogy and Petrology 162, 133–151.

Lyakhovsky, V., Hurwitz, S., Navon, O., 1996. Bubble growth in rhyolitic melts: experimental and numerical investigation. Bulletin of Volcanology 58, 19–32.

Mangan, M., Sisson, T., 2000. Delayed, disequilibrium degassing in rhyolite magma: decompression experiments and implications for explosive volcanism. Earth and Planetary Science Letters 183, 441–455.

Mangan, M., Sisson, T., 2005. Evolution of melt-vapor surface tension in silicic volcanic systems: Experiments with hydrous melts. Journal of Geophysical Research 110, B01202. doi:10.1029/2004JB003215

Mangan, M.T., Sisson, T.W., Hankins, W.B., 2004. Decompression experiments identify kinetic controls on explosive silicic eruptions. Geophysical Research Letters 31, L08605. doi:10.1029/2004GL019509

Marianelli, P., Sbrana, A., Metrich, N., Cecchetti, A., 2005. The deep feeding system of Vesuvius involved in recent violent strombolian eruptions. Geophysical Research Letters 32, L02306. doi:10.1029/2004GL021667

Martel, C., Iacono-Marziano, G., 2015. Timescales of bubble coalescence, outgassing, and foam collapse in decompressed rhyolitic melts. Earth and Planetary Science Letters 412, 173–185.

Masotta, M., Ni, H., Keppler, H., 2014. In situ observations of bubble growth in basaltic, andesitic and rhyodacitic melts. Contributions to Mineralogy and Petrology 167, 1–14.

Massol, H., Koyaguchi, T., 2005. The effect of magma flow on nucleation of gas bubbles in a volcanic conduit. Journal of Volcanology and Geothermal Research 143, 69–88.

Métrich, N., Wallace, P.J., 2008. Volatile abundances in basaltic magmas and their degassing paths tracked by melt inclusions. Reviews in Mineralogy and Geochemistry 69, 363–402.

Métrich, N., Bertagnini, A., Di Muro, A., 2010. Conditions of magma storage, degassing and ascent at Stromboli: new insights into the volcano plumbing system with inferences on the eruptive dynamics. Journal of Petrology 51, 603–626.

Métrich, N., Bertagnini, A., Landi, P., Rosi, M., 2001. Crystallization driven by decompression and water loss at Stromboli volcano (Aeolian Islands, Italy). Journal of Petrology 42, 1471–1490.

Métrich, N., Bertagnini, A., Landi, P., Rosi, M., Belhadj, O., 2005. Triggering mechanism at the origin of paroxysms at Stromboli (Aeolian Archipelago, Italy): the 5 April 2003 eruption. Geophysical Research Letters 32, L103056. doi:10.1029

Mourtada-Bonnefoi, C.C., Laporte, D., 1999. Experimental study of homogeneous bubble nucleation in rhyolitic magmas. Geophysical Research Letters 26, 3505–3508.

Mourtada-Bonnefoi, C.C., Laporte, D., 2002. Homogeneous bubble nucleation in rhyolitic magmas: an experimental study of the effect of H_2O and CO_2. Journal of Geophysical Research 107, B4. doi:10.1029/2001JB00290

Mourtada-Bonnefoi, C.C., Laporte, D., 2004. Kinetics of bubble nucleation in a rhyolitic melt: an experimental study of the effect of ascent rate. Earth and Planetary Science Letters 218, 521–537.

Newman, S., Lowenstern, J.B., 2002. VolatileCalc: a silicate melt–H_2O–CO_2 solution model written in Visual Basic for Excel. Computers & Geosciences 28, 597–604.

Pichavant, M., Pompilio, M., D'Oriano, C., Di Carlo, I., 2011. Petrography, mineralogy and geochemistry of a primitive pumice from Stromboli: implications for the deep feeding system. European Journal of Mineralogy 23, 499–517.

Pichavant, M., Di Carlo, I., Le Gac, Y., Rotolo, S.G., Scaillet, B., 2009. Experimental constraints on the deep magma feeding system at Stromboli volcano, Italy. Journal of Petrology 50, 601–624.

Pichavant, M., Di Carlo, I., Rotolo, S.G., Scaillet, B., Burgisser, A., Le Gall, N., Martel, C., 2013. Generation of CO_2-rich melts during basalt magma ascent and degassing. Contributions to Mineralogy and Petrology 166, 545–561.

Pioli, L., Erlund, E., Johnson, E., Cashman, K., Wallace, P., Rosi, M., Granados, H.D., 2008. Explosive dynamics of violent Strombolian eruptions: the eruption of Parícutin Volcano 1943–1952 (Mexico). Earth and Planetary Science Letters 271, 359–368.

Polacci, M., Baker, D.R., Bai, L., Mancini, L., 2008. Large vesicles record pathways of degassing at basaltic volcanoes. Bulletin of Volcanology 70, 1023–1029.

Polacci, M., Baker, D.R., Mancini, L., Tromba, G., Zanini, F., 2006. Three-dimensional investigation of volcanic textures by X-ray microtomography and implications for conduit processes. Geophysical Research Letters 33, L13312. doi:10.1029/2006GL026241

Polacci, M., Baker, D.R., Mancini, L., Favretto, S., Hill, R.J., 2009. Vesiculation in magmas from Stromboli and implications for normal Strombolian activity and paroxysmal explosions in basaltic systems. Journal of Geophysical Research 114, B01206. doi:10.1029/2008JB005672

Proussevitch, A.A., Sahagian, D.L., Tsentalovich, E.P., 2007. Statistical analysis of bubble and crystal size distributions: Formulations and procedures. Journal of Volcanology and Geothermal Research 164, 95–111.

Richet, P., Whittington, A., Holtz, F., Behrens, H., Ohlhorst, S., Wilke, M., 2000. Water and the density of silicate glasses. Contributions to Mineralogy and Petrology 138, 337–347.

Sable, J.E., Houghton, B.F., Del Carlo, P., Coltelli, M., 2006. Changing conditions of magma ascent and fragmentation during the Etna 122 BC basaltic Plinian eruption: evidence from clast microtextures. Journal of Volcanology and Geothermal Research 158, 333–354.

Sable, J.E., Houghton, B.F., Wilson, C.J.N., Carey, R.J., 2009. Eruption mechanisms during the climax of the Tarawera 1886 basaltic Plinian eruption inferred from microtextural characteristics of the deposits. Studies in volcanology. The legacy of George Walker. Geological Society, London 129–154.

Shea, T., Houghton, B.F., Gurioli, L., Cashman, K.V., Hammer, J.E., Hobden, B.J., 2010. Textural studies of vesicles in volcanic rocks: an integrated methodology. Journal of Volcanology and Geothermal Research 190, 271–289.

Shishkina, T.A., Botcharnikov, R.E., Holtz, F., Almeev, R.R., Portnyagin, M.V., 2010. Solubility of H_2O-and CO_2-bearing fluids in tholeiitic basalts at pressures up to 500MPa. Chemical Geology 277, 115–125.

Simakin, A.G., Armienti, P., Epel'baum, M.B., 1999. Coupled degassing and crystallization: experimental study at continuous pressure drop, with application to volcanic bombs. Bulletin of Volcanology 61, 275–287.

Sparks, R.S.J., 1978. The dynamics of bubble formation and growth in magmas: a review and analysis. Journal of Volcanology and Geothermal Research 3, 1–37.

Sparks, R.S.J., Barclay, J., Jaupart, C.P.M.A., Mader, H.M., Phillips, J.C., 1994. Physical aspects of magma degassing I. Experimental and theoretical constraints on vesiculation. American Society of Mineralogy Reviews 30, 413–445.

Spilliaert, N., Allard, P., Métrich, N., Sobolev, A.V., 2006. Melt inclusion record of the conditions of ascent, degassing, and extrusion of volatile-rich alkali basalt during the powerful 2002 flank eruption of Mount Etna (Italy). Journal of Geophysical Research 111, B04203. doi:10.1029/2005JB003934

Taylor, J.R., Wall, V.J., Pownceby, M.I., 1992. The calibration and application of accurate redox sensors. American Mineralogist 77, 284–295.

Toramaru, A., 1989. Vesiculation process and bubble size distributions in ascending magmas with constant velocities. Journal of Geophysical Research 94, 17523–17542.

Toramaru, A., 1995. Numerical study of nucleation and growth of bubbles in viscous magmas. Journal of Geophysical Research 100, 1913–1931.

Toramaru, A., 2006. BND (bubble number density) decompression rate meter for explosive volcanic eruptions. Journal of Volcanology and Geothermal Research 154, 303–316.

Toramaru, A., 2014. On the second nucleation of bubbles in magmas under sudden decompression. Earth and Planetary Science Letters 404, 190–199.

Witham, F., 2011. Conduit convection, magma mixing, and melt inclusion trends at persistently degassing volcanoes. Earth and Planetary Science Letters 301, 345–352.

Yamada, K., Tanaka, H., Nakazawa, K., Emori, H., 2005. A new theory of bubble formation in magma. Journal of Geophysical Research 110, B02203. doi:10.1029/2004JB003113

Yoshimura, S., 2015. Diffusive fractionation of H_2O and CO_2 during magma degassing. Chemical Geology 411, 172–181.

Zhang, Y., Stolper, E.M., 1991. Water diffusion in a basaltic melt. Nature 351, 306–309.

Zhang, Y., Ni, H., 2010. Diffusion of H, C, and O components in silicate melts. Reviews in Mineralogy and Geochemistry 72, 171–225.

Figure captions

Fig. 1 Three dimensional representations of the samples and methods of vesicularity determination used in this study. V: total volume investigated; v2: void space volume; v3: melt volume; v4: bubble volume. (a) Vesicularity (V^c, Tables 3 and 4) determined from the total sample volume V (V^c = 100*v4/(v3+v4)), see text for the determination of v3 and v4. (b) Vesicularity (V^d, Tables 3 and 4) determined from a delimited sub-volume V_{sub} (V^d = 100*v4/(v3+v4)), see text for the determination of v4. The open bubbles located at the rim of the glass cylinder appear in black in both (a) and (b). In (a), these are considered as voids (v2), while in (b) these are counted as bubbles (v4). In (a), the trace of the sub-volume is delimited by the dashed square.

Fig. 2 Representative textures of post-decompression glasses. (a) Detailed transmitted light microscopic photograph of a double-polished section of a sample (D31#3, P_f = 150 MPa) showing a homogeneous distribution of newly formed small (< 5 μm) bubbles and no oxides or obvious heterogeneities which could have facilitated their nucleation. (b) Tomographic slice of a sample quenched at a pressure above the critical pressure of homogeneous bubble nucleation (sample D31#2, P_f = 150 MPa): the sample is bubble-free. (c) Tomographic slice of a sample quenched at a pressure just below the pressure of homogeneous bubble nucleation (sample D34#2, P_f = 100 MPa): the sample is densely vesiculated with small and almost homogeneously distributed bubbles. The black arrow indicates the bubbly rim. See Table 3 for details about the experimental conditions and textural results.

Fig. 3 (a) Vesicularity *V*, (b) average bubble diameter *D* and (c) bubble number density per unit volume of melt BND_{melt} plotted as a function of final pressure P_f for the post-decompression glasses of this study. Experimental data in Tables 3 and 4. For the partially fragmented sample S+D38#1, data from the unfragmented part are from Table 4. See text for bubble diameters in the fragmented part. The three glass series are distinguished (see text). Series #1: black circles; series #2: gray circles; series #3: white circles. In (a), equilibrium vesicularities (thick black and gray lines) calculated respectively for pure H_2O and CO_2 degassing (see text) are shown for comparison with the experimental data. The *V*, *D* and BND_{melt} values for Strombolian pumices and Masaya clasts (for this one only BND_{melt} values are shown) are plotted (data come from Polacci et al., 2006, 2009 and Costantini et al., 2010, respectively) for comparison with the experimental data points.

Fig. 4 Bubble textures of series (a) #1, (b) #2 and (c) #3 glasses decompressed to 25 MPa P_f. Evolution of the bubble size distribution (BSD) with decreasing pressure in series (d) #1, (e) #2 and (f) #3 post-decompression glasses. For each series, two post-decompression glasses are detailed, one representative of the early and the other of the late stage of the nucleation process. Histograms show frequencies (normalized to 100) of individual bubble diameters in the glass population using size classes of 10 µm each. Numbers in parentheses are bubble numbers for each population (*n* in Tables 3 and 4). Details about experimental conditions and other textural data in Tables 3 and 4.

Fig. 5 H_2O and CO_2 concentrations in glasses from the synthesis and decompression experiments. Black symbols: series #1 glasses; gray symbols: series #2 glasses; white symbols: series #3 glasses. Circles: pre-decompression glasses synthesized at 200 MPa P_{in} (initial pressure); rectangles: glasses decompressed to 150 MPa P_f (final pressure); triangles: glasses decompressed to 100 MPa P_f; squares: glasses decompressed to 50 MPa P_f; diamonds: glasses decompressed to 25 MPa P_f. Error bars (standard deviations, Table 5) are indicated on the data points. Thin continuous lines: fluid-melt equilibrium saturation isobars (25–250 MPa); dashed curves: equilibrium decompression paths calculated for a series #2 and a series #3 pre-decompression melt assuming closed-system behavior. Isobars and decompression paths both calculated with VolatileCalc (Newman and Lowenstern, 2002).

Fig. 6 H_2O distribution profiles measured in the series #1 glasses decompressed to 150–25 MPa P_f, perpendicular to the long axis of the cylinder as a function of the distance from the edge. The farthest point of each FTIR profile was acquired as close as possible to the other edge. Average H_2O concentration data are given in Table 5. (a) H_2O supersaturation vs. distance plot. H_2O supersaturation is defined relative to the H_2O solubility at each P_f (Lesne et al., 2011b) as: H_2O supersaturation = measured melt H_2O concentration at a specific position – H_2O solubility. The dashed horizontal line (H_2O supersaturation = 0) represents the solubility values for each P_f. Note that three profiles are available for the 25 MPa P_f charge (S+D38#1). The H_2O distribution profile for sample D10#1 (P_f = 50 MPa) is illustrated in (b).

Fig. 7 Typical coalescence structures frozen in sample S+D38#1 decompressed to 25 MPa P_f. Inter-bubble melt films (IBFs) are thinned by stretching (a), bending (b), and dimpling (c, d) (see also Castro et al., 2012; Martel and Iacono-Marziano, 2015). See Table 4 for experimental conditions.

Fig. 8 H_2O (a) and CO_2 (b) concentrations in post-decompression glasses (Table 5) plotted as a function of vesicularity (expressed as vol% bubbles, V^d in Tables 3 and 4). In (a), only data for series #1 and #2 glasses are shown and data for series #2 and #3 in (b). Black symbols: series #1 glasses; gray symbols: series #2 glasses; white symbols: series #3 glasses. Rectangles: glasses decompressed to 150 MPa P_f (final pressure); triangles: glasses decompressed to 100 MPa P_f; squares: glasses decompressed to 50 MPa P_f; diamonds: glasses decompressed to 25 MPa P_f. Dashed horizontal lines: pure H_2O (a) and CO_2 (b) solubilities for each P_f (Lesne et al., 2011a, b). Error bars (standard deviations, Table 5) are indicated within the data points.

Fig. 9 Cumulative *BND* plots. Bubble size distributions (BSD) expressed as log-log plots of bubble number density (BND_{melt}, in mm^{-3}) vs. bubble volume for all post-decompression glasses from this study. For each glass sample, the bubble population is characterized by a range of bubble size (expressed as diameters in Tables 3 and 4) and a bubble number density value (Tables 3 and 4). Each point along the distribution curve corresponds to the number of bubbles with a volume strictly larger than a given volume. (a) Series #1 glasses, (b) series #2 glasses, (c) series#3 glasses. Rectangles: glasses decompressed to 150 MPa P_f (final pressure); triangles: glasses decompressed to 100 MPa P_f; squares: glasses decompressed to 50 MPa P_f; diamonds: glasses decompressed to 25 MPa P_f. The continuous lines are power law fits and the continuous curves are exponential fits, both regressed with Excel software. α is the power law exponent.

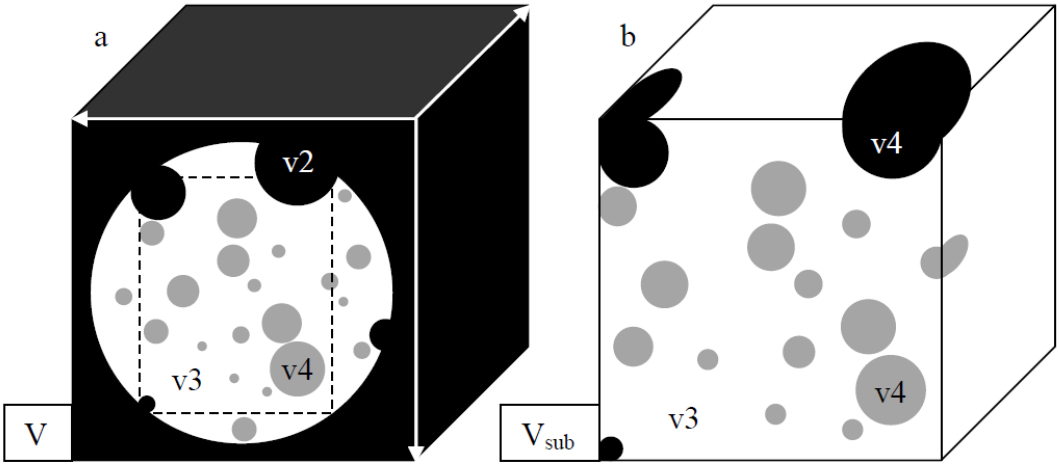

Figure 1

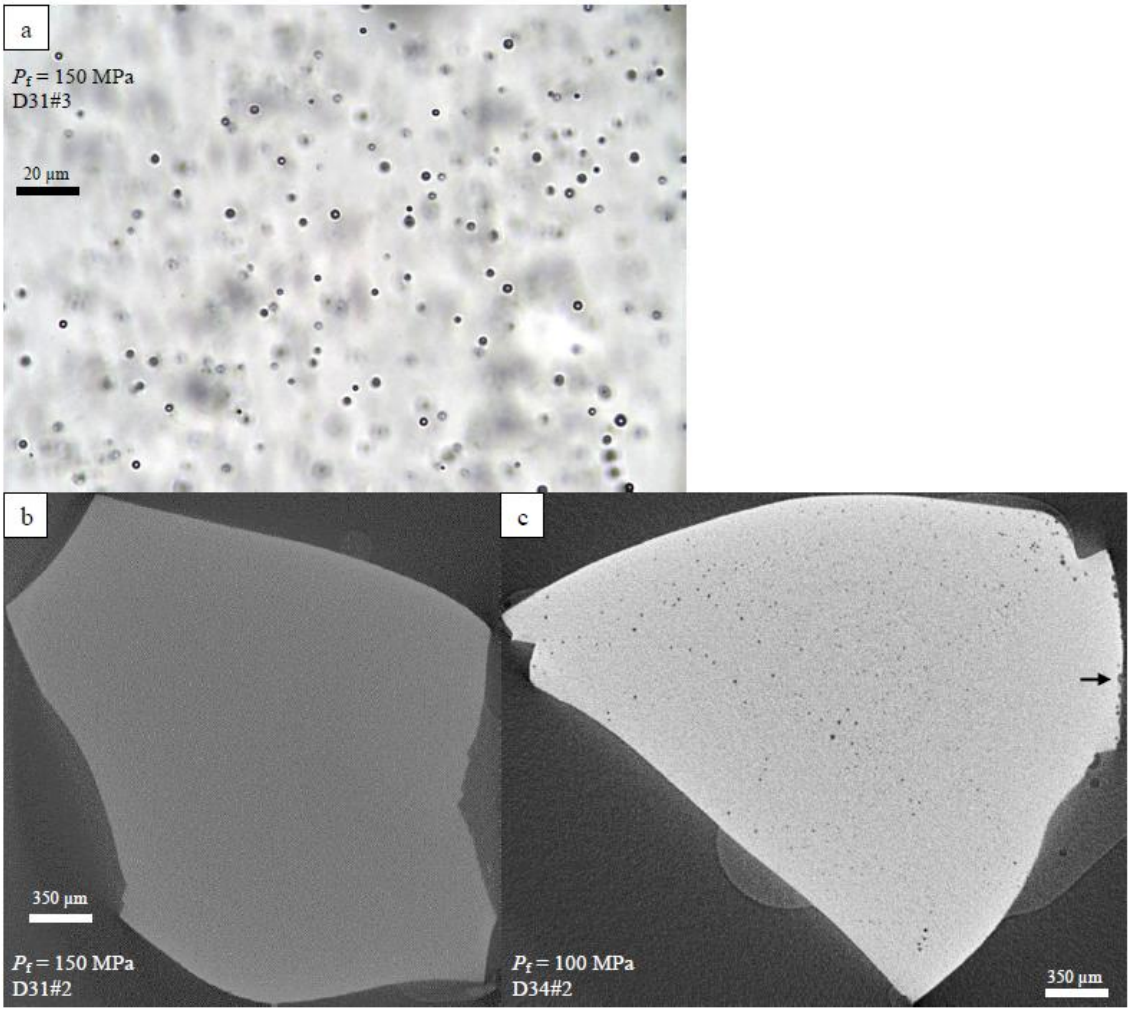

Figure 2

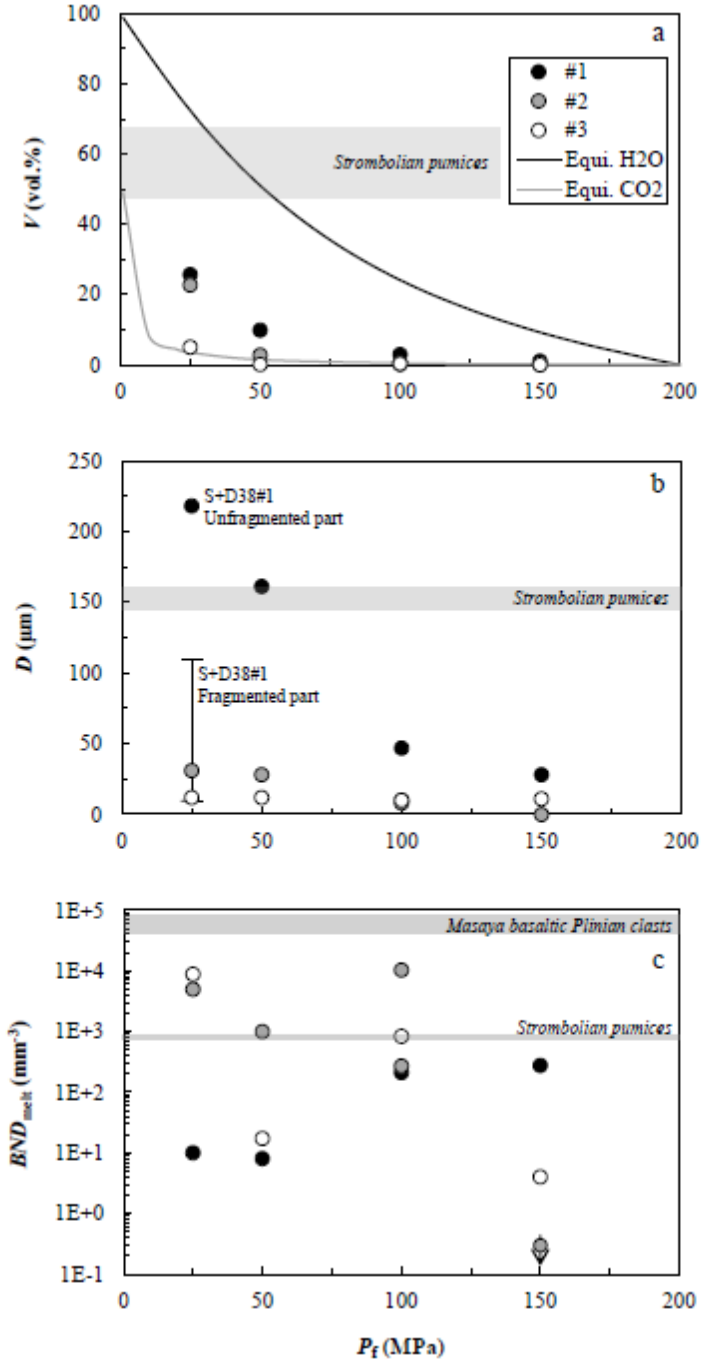

Figure 3

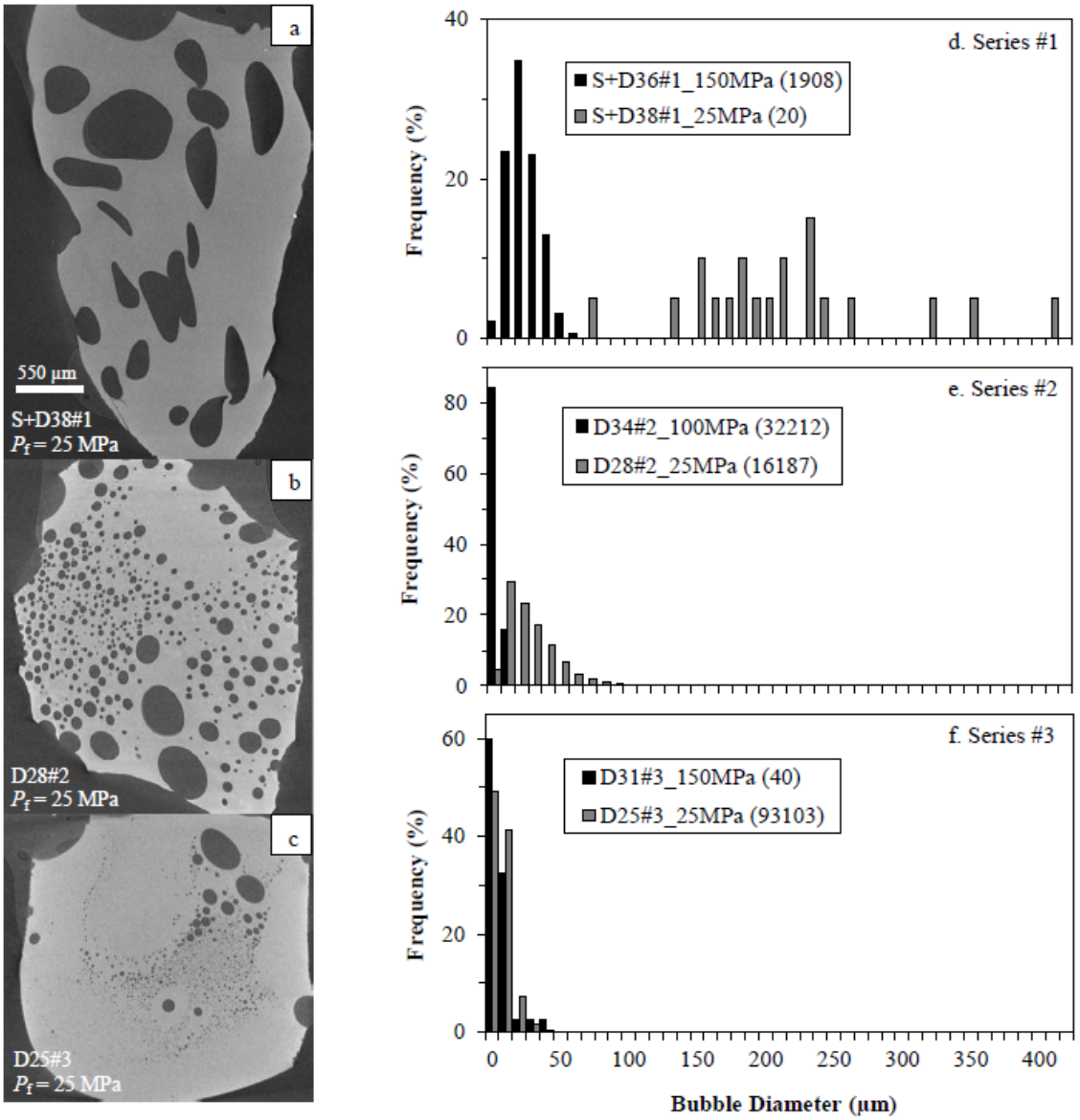

Figure 4

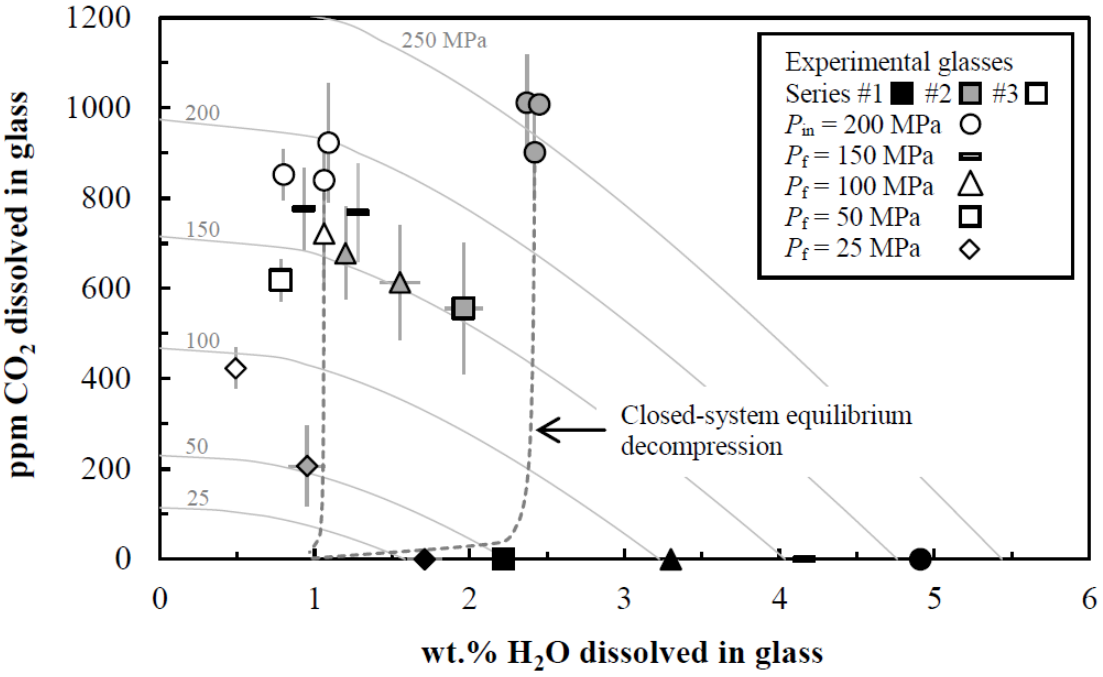

Figure 5

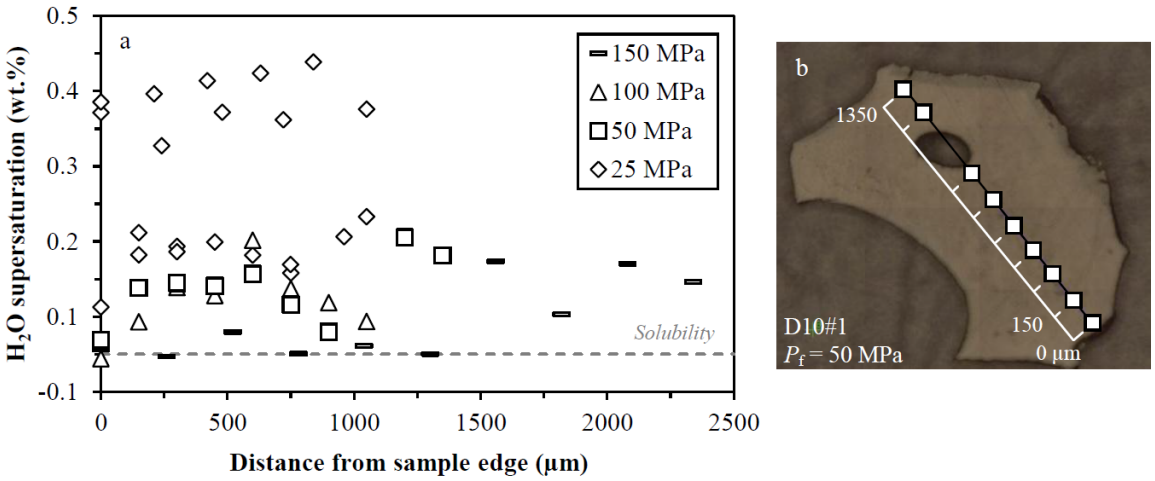

Figure 6

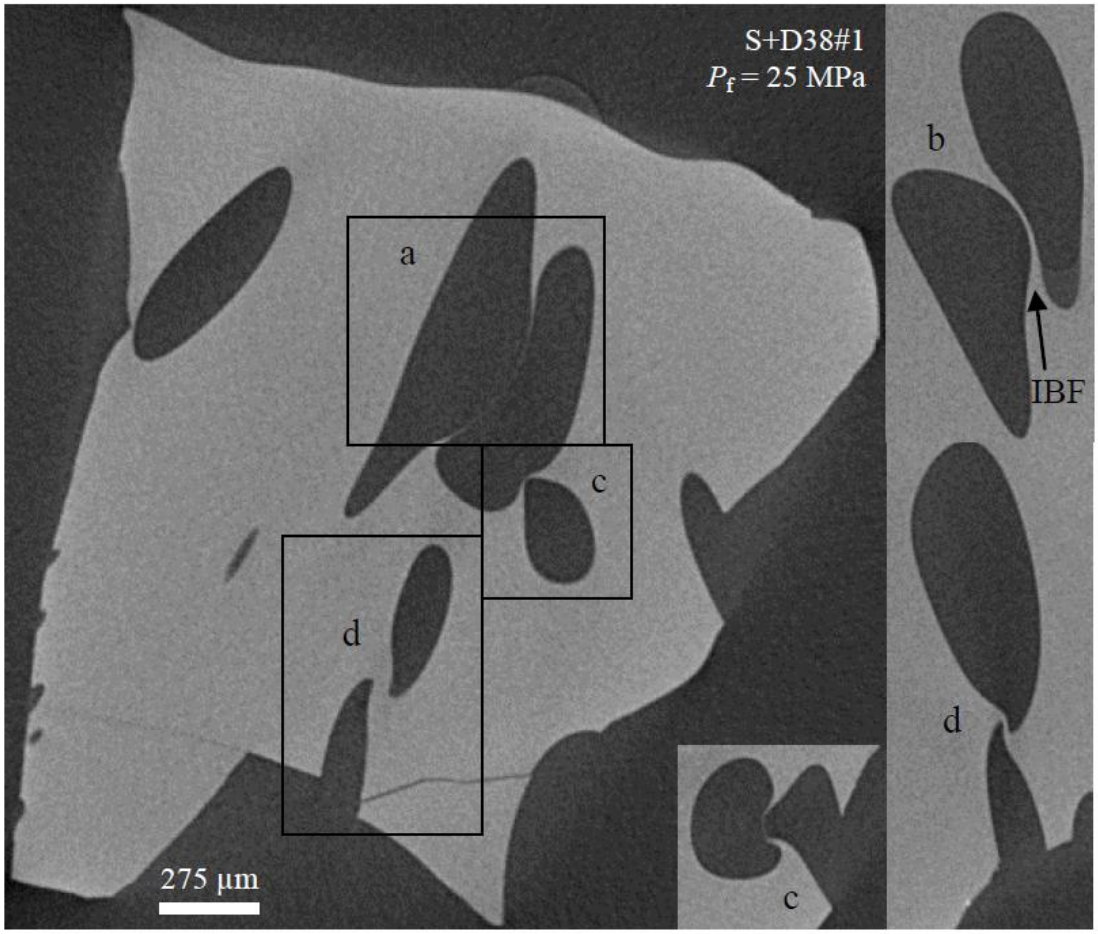

Figure 7

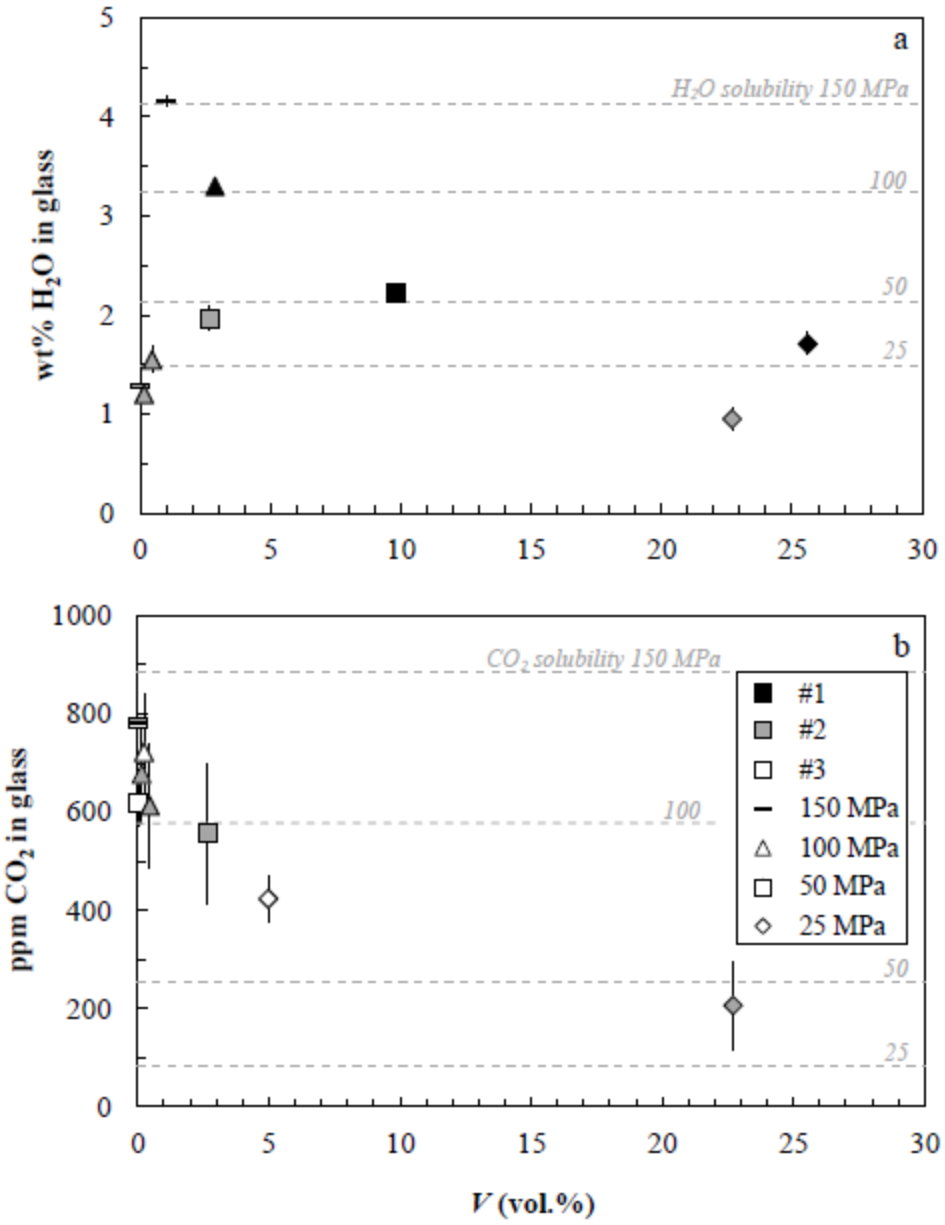

Figure 8

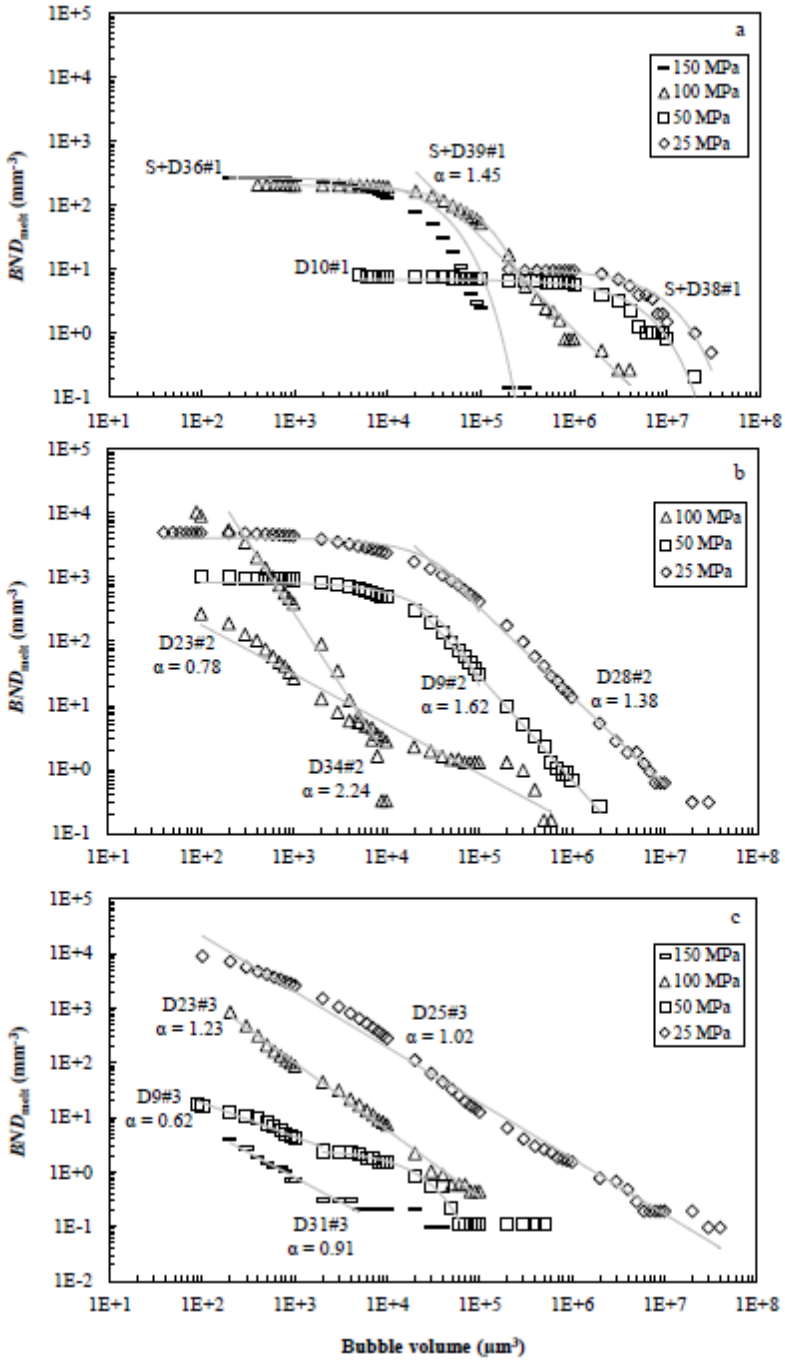

Figure 9

Table 1. Composition of PST-9 golden pumice and starting glass

Label	PST-9[a]	Glass[b] (*n* = 54)
SiO_2	49.4	50.9 (3)[c]
TiO_2	0.79	0.81 (8)
Al_2O_3	15.75	15.99 (28)
Fe_2O_3	1.3	nd
FeO	6.5	7.7 (6)
MnO	0.15	0.16 (8)
MgO	7.96	7.21 (41)
CaO	12.73	12.34 (24)
Na_2O	2.27	2.39 (9)
K_2O	1.85	1.90 (12)
P_2O_5	0.43	0.55 (17)
Cr_2O_3	–	0.03 (4)
NiO	–	0.05 (6)
Total	99.1	97.4 (10)

[a] Whole-rock analysis (from Di Carlo et al., 2006). Major elements (wt.%) analyzed by inductively coupled plasma atomic emission spectrometry (ICP-AES); total includes LOI (loss of ignition) = 0.62 wt.%; trace elements analyzed by inductively coupled plasma mass spectrometry (ICP-MS; Cr 259 ppm; Ni 75 ppm; Ba 920 ppm; La 45 ppm; Eu 2.0 ppm; Lu 0.3 ppm). Analysis performed at the Centre de Recherches Pétrographiques et Géochimiques (CRPG, Nancy, France).

[b] Electron microprobe analysis (normalized to 100%) of PST-9 glass, with all Fe reported as FeO; oxides are in wt.%.

[c] One standard deviation in terms of last digit.

n: number of analyses.

nd: not determined.

Table 2. Synthesis experiments

Run	XH_2O_{in}	*T* (°C)	*P* (MPa)	*t* (min)	H_2O glass (wt.%)	CO_2 glass (ppm)
Volatile: H_2O (#1)						
S9#1	1	1200	201.8	2795	4.91 (1)	0 (0)
Volatile: H_2O+CO_2 (#2)						
S6#2	0.56	1200	202.2	2760	2.37 (1)	1011 (106)
S13#2	0.58	1200	201.5	2878	2.45 (2)	1008 (21)
S16#2	0.59	1200	201.8	2873	2.42 (3)	901 (104)
Volatile: H_2O+CO_2 (#3)						
S6#3	0	1200	202.2	2760	0.80 (3)	852 (57)
S13#3	0	1200	201.5	2878	1.09 (3)	923 (132)
S16#3	0	1200	201.8	2873	1.06 (1)	840 (64)

XH_2O_{in} = initial molar H_2O / (H_2O + CO_2) added in the charge.

T: run temperature; *P*: run pressure; *t*: duration of the synthesis experiment.

Table 3. Decompression experiments: run conditions and textural information

Sample	Starting glass	P_{in} (MPa)	P_f (MPa)	t_{ramp} (s)	|dP/dt| (kPa/s)	Bubble 3D characteristics										
						n	pk. size (µm)	range (µm)	*D* (µm)	*BND*[a] (mm^{-3})	BND_{melt}[b] (mm^{-3})	*S* (µm)	V^c (vol.%)	V^d (vol.%)	$V_{Equi.\ H2O}$ (vol.%)	$V_{Equi.\ CO2}$ (vol.%)
Volatile: H_2O (#1)																
D10#1	S9#1	200	50	1928	78	38	–	22–368	161	7.8	8.1	309	2.93	9.85	51.0	
Volatile: H_2O+CO_2 (#2)																
D31#2	S16#2	200	150	642	78	0	–	–	0	0.0	0.0	–	0.00	0.00	9.22	0.17
D23#2	S13#2	200	100	1344	78	1692	7	7–109	10	269	269	96	0.07	0.15	24.1	0.47
D34#2	S13#2	200	100	1344	78	32212	6	6–27	8	10297	10331	28	0.32	0.46	24.1	0.47
D9#2	S6#2	200	50	1928	78	11609	23	6–169	28	970	991	62	2.19	2.67	51.0	1.48
D28#2	S16#2	200	25	2372	78	16187	16	4–424	31	4069	4935	36	17.5	22.7	72.5	3.47
Volatile: H_2O+CO_2 (#3)																
D31#3	S16#3	200	150	642	78	40	8	8–42	11	4.0	4.0	391	0.00	0.00	9.22	0.17
D23#3	S13#3	200	100	1344	78	5768	7	7–71	10	836	836	66	0.07	0.24	24.1	0.47
D9#3	S6#3	200	50	1928	78	160	6	6–102	12	17	17	96	0.01	0.02	51.0	1.48
D25#3	S13#3	200	25	2372	78	93103	8	6–425	12	8569	8799	30	2.60	4.97	72.5	3.47

P_{in} (initial pressure): pressure at the beginning of decompression ramp; P_f (final pressure): pressure at which the experiment was quenched; t_{ramp}: duration of the ramp; |dP/dt|: decompression/ascent rate ($=10^6(P_{in}-P_f)/(g d t_{ramp})$), with g = 9.81 m/s^2 and d = 2650 kg/m^3.

X-ray microtomographic data acquired on entire charges (except V^{d}).

n: number of bubbles counted in the analyzed volume.

pk. size: main peak diameter in bubble size distribution histograms.

range: total range of bubble diameters.

D: average bubble diameter.

[a] *BND*: bubble number density expressed in number of bubbles per mm^3 of the total sample (glass + bubbles).

[b] BND_{melt}: bubble number density per melt volume (without bubbles, following Proussevitch et al., 2007).

S: average spacing between bubbles calculated from BND_{melt} ($S = (3/4\pi BND_{melt})^{1/3}$; Lyakhovsky et al., 1996; Baker et al., 2006).

[c] *V*: vesicularity (volume fraction of bubbles, vol.%) measured from the total sample.

[d] *V*: vesicularity measured from representative sub-volumes.

$V_{Equi.H2O}$ and $V_{Equi.CO2}$: equilibrium vesicularities computed for the PST-9 composition considering the degassing of pure H_2O and pure CO_2, respectively (see text).

Table 4. Synthesis + Decompression experiments: run conditions and textural information

Sample	P_{in} (MPa)	t (min)	P_f (MPa)	t_{ramp} (s)	|dP/dt| (kPa/s)	Bubble 3D characteristics						
						n	pk. size (µm)	range (µm)	D (µm)	BND[a] (mm^{-3})	BND_{melt}[b] (mm^{-3})	S (
Volatile: H_2O (#1)												
S+D36#1	202.0	41	150	642	78	1908	25	8–86	28	274	275	9
S+D39#1	202.2	54	100	1344	78	776	43	10–190	47	207	210	1
S+D38#1	202.2	60	25	2372	78	20	–	76–414	218	9.3	10	2

The synthesis + decompression experiments are divided in two steps: synthesis at P_{in} and decompression between P_{in} and P_f. P_{in} (initial pressure): pressure at the beginning of decompression ramp; t: duration of the synthesis step; P_f (final pressure): pressure at which the experiment was quenched; t_{ramp}: duration of the decompression step; |dP/dt|: decompression rate ($=10^6(P_{in}-P_f)/(gdt_{ramp})$), with g = 9.81 m/s^2 and d = 2650 kg/m^3.

X-ray microtomographic data acquired on entire charges (except V^d).

Bubble 3D characteristics abbreviations as in Table 3.

S+D38#1 X-ray CT data concern the unfragmented part of the charge.

Table 5. FTIR data

Glass	n^a	Thickness (µm)	Absorbance 3530 cm^{-1}	H_2O (wt.%)	Absorbance 1515 cm^{-1}	CO_2 (ppm)
Synthesis experiments						
Volatile: H_2O (#1)						
S9#1	6	29 (2)[b]	1.337 (94)	4.91 (1)		
Volatile: H_2O+CO_2 (#2)						
S6#2	5	31 (1)	0.698 (34)	2.37 (1)	0.070 (9)	1011 (106)
S13#2	7	42 (2)	0.976 (44)	2.45 (2)		
	7	52 (5)			0.118 (13)	1008 (21)
S16#2	6	32 (2)	0.734 (50)	2.42 (3)	0.065 (11)	901 (104)
Volatile: H_2O+CO_2 (#3)						
S6#3	7	149 (1)	1.147 (48)	0.80 (3)	0.287 (18)	852 (57)
S13#3	8	111 (5)	1.168 (75)	1.09 (3)		
	5	62 (4)			0.129 (21)	923 (132)
S16#3	8	48 (3)	0.496 (34)	1.06 (1)	0.092 (12)	840 (64)
Decompression experiments						
Volatile: H_2O (#1)						
D10#1	9	72 (5)	1.523 (85)	2.22 (4)		
Volatile: H_2O+CO_2 (#2)						
D31#2	10	55 (5)	0.675 (69)	1.28 (5)	0.098 (20)	786 (108)
D23#2	5	84 (1)	0.973 (19)	1.20 (3)		
	7	68 (4)			0.105 (18)	678 (103)
D34#2	7	118 (5)	1.752 (132)	1.55 (13)		
	11	47 (3)			0.066 (16)	613 (127)
D9#2	12	58 (2)	1.059 (92)	1.91 (15)	0.088 (15)	668 (120)
	13	56 (1)	1.074 (50)	2.00 (6)	0.057 (8)	452 (65)
	av.			1.96 (12)		556 (144)
D28#2	9	61 (6)	0.566 (84)	0.95 (12)	0.029 (13)	206 (89)
Volatile: H_2O+CO_2 (#3)						
D31#3	11	152 (8)	1.384 (90)	0.93 (1)	0.269 (37)	777 (90)
D23#3	10	133 (7)	1.365 (73)	1.06 (2)	0.219 (43)	722 (119)
D9#3	8	171 (1)	1.291 (65)	0.78 (4)	0.239 (19)	619 (46)
D25#3	7	73 (4)	0.350 (40)	0.49 (4)		
	6	123 (9)			0.118 (14)	423 (45)
Synthesis+Decompression experiments						
Volatile: H_2O (#1)						
S+D36#1	10	38 (5)	1.480 (184)	4.16 (5)		
S+D39#1	8	58 (1)	1.801 (49)	3.30 (5)		
S+D38#1	11	54 (3)	0.932 (58)	1.80 (6)		
	10	102 (7)	1.590 (92)	1.61 (3)		
	av			1.71 (11)		

.

D9#2 and S+D38#1 analyzed in duplicate. Average H_2O and CO_2 concentrations (av.) and standard deviations are reported. These are calculated by using all analytical spots.

[a] Number of analytical spots.

[b] One standard deviation in terms of the last digit.

Highlights

- Decompressions provide information on homogenous bubble nucleation in basalts
- Use of volatile-bearing melt compositions to simulate magma ascent at Stromboli
- Significant effect of CO_2 on physical mechanisms of basaltic melt degassing
- Both near-equilibrium and disequilibrium degassing occur in our experiments
- Decompression textures approach those of basaltic products from explosive eruptions